Eddy Energetics in the Upper Equatorial Pacific during the Hawaii-to-Tahiti Shuttle Experiment

DOUGLAS S. LUTHER AND ERIC S. JOHNSON

Scripps Institution of Oceanography, University of California, San Diego, La Jolla, California

(Manuscript received 16 December 1988, in final form 25 October 1989)

ABSTRACT

Eddy energetics in the central equatorial Pacific Ocean is examined using Acoustic Doppler Current Profiler velocities and CTD densities collected during the Hawaii-to-Tahiti Shuttle Experiment, in 1979–80. Three distinct sources of eddy energy are identified with varying degrees of statistical reliability, and are interpreted as evidence for three separate instabilities of the mean flow field. An instability at and just north of the equator occurs primarily in boreal summer and fall. It arises from the cyclonic shear between the Equatorial Undercurrent and the South Equatorial Current (SEC) north of the equator. The instability is present only when and where both currents are well developed, and there is little involvement of the shear between the SEC and the North Equatorial Countercurrent (NECC). The instability is characterized by local maxima in zonal and meridional eddy velocity variance, strong $\overline{U^*V^*}$ Reynolds stress, and large mean flow to eddy kinetic energy conversion. Despite seasonal variability of the eddy kinetic energy production, no annual cycle energy is converted to eddy energy. A second instability occurs at the equatorial front at 3°N to 6°N, primarily during boreal winter. The instability is identified by large mean-to-eddy potential energy conversion. Finally, a third instability is evidenced by strong downgradient (northward) eddy heat flux and large mean flow to eddy potential energy conversion in the thermocline of the NECC during boreal spring. Both features are confined below 60 m at 5°N–9°N. While the eddies gain potential energy from these last two instabilities, they are losing kinetic energy to the mean flow at a somewhat slower rate.

Nonlinear advection appears to be unimportant in the total eddy energy balance, but the meridional diffusion of eddy energy represented by the meridional divergence of eddy pressure work is large and significant. The latter redistributes eddy energy into (not out of) the region of the barotropic instability just north of the equator.

1. Introduction

Energetic, mesoscale perturbations of currents and temperature in the upper equatorial oceans appear to play significant roles in the mean balances of momentum, heat and energy. First documented by Düing et al. (1975) and Legeckis (1977), the perturbations often appear to be wavelike, with varying degrees of nonlinearity, having periods and wavelengths on the order of 10 days and 1000 km, respectively, compared to 100 days and 100 km for midlatitude mesoscale perturbations. For the sake of brevity, these perturbations will be referred to as eddies, but this should not be construed as a judgment as to their dynamic character. An example of the variability extant during the collection of the Acoustic Doppler Current Profiler (ADCP) data discussed in this paper is provided by Fig. 1. Hansen and Paul (1984) and Weisberg (1987) have reviewed many of the observations of mesoscale eddies in the Pacific and Atlantic oceans, and have reviewed the theories of their generation by instabilities of the mean zonal currents. Despite the emphasis on such instability theories in the recent literature, not all, nor probably even most, of the mesoscale fluctuations throughout the equatorial oceans owe their existence to instabilities of the mean zonal currents. Other forcing mechanisms include the stresses applied at the water–air interface by surface winds, and instabilities of boundary currents (e.g., Fantini and Tung 1987, and Kindle and Thompson 1989). Only the eddy variability in specific longitude bands of the upper equatorial Pacific and Atlantic oceans has been clearly linked to instabilities of the mean zonal currents. Since the present ADCP dataset was collected within such a longitude band, models of these instabilities are worth summarizing.

Philander (1976, 1978) produced a two-layer model of the stability of idealized mean zonal currents near the equator which yielded unstable modes that derived their energy principally from a barotropic instability arising from the strong meridional shear between the westward South Equatorial Current (SEC) and the eastward North Equatorial Countercurrent (NECC); consequently only horizontal Reynolds stresses were important. A multilevel numerical model by Cox (1980) confirmed the dominance of barotropic insta-

Corresponding author address: Dr. Douglas S. Luther, Scripps Institution of Oceanography, A-030, University of California, La Jolla, CA 92093.

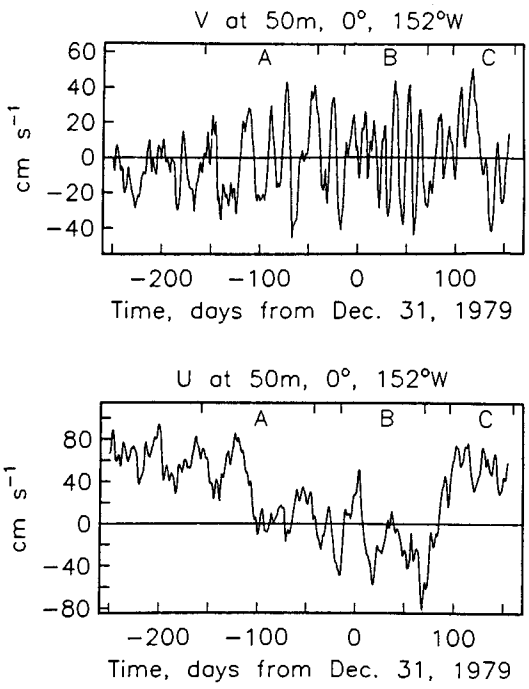

FIG. 1. The moored current meter (MCM) velocities recorded at 50 m depth on the equator at 152°W during the Shuttle Experiment. Note the large annual variability in U, the energetic higher frequency fluctuations in both U and V, and the difference in the typical frequency of the dominant V fluctuations found before and after December 1979. The significance of the time periods, A, B and C is discussed in section 6.

bility while also noting that baroclinic instability and vertical Reynolds stresses contributed significantly to the growth of the eddies. Semtner and Holland's (1980) multilevel numerical model, which totally lacked a NECC, produced mesoscale eddies by baroclinic instability, although a longer period meander of the Equatorial Undercurrent (EUC) was generated by a barotropic instability of that current.

In both the Pacific and the Atlantic, the kinematic characteristics of the fluctuations have been described and the barotropic energy source confirmed, primarily with near-equatorial current meter data (Weisberg 1984; Philander et al. 1985; Lukas 1987; Weisberg and Weingartner 1988), but also with surface drift buoy data (Hansen and Paul 1984) which allowed the meridional structures of eddy energy and the energy production to be calculated, at least for one depth near the surface. Contrary to Philander's (1976, 1978) early theories, the strongest barotropic eddy energy production appears to be located (Hansen and Paul 1984) on the south side of the strong Northern Hemisphere branch of the SEC (hereafter, referred to as SECN) rather than the north side. Despite this, Philander's (1978) analytical calculation of the period and wavelength of the most unstable mode matches the observations quite closely.

The role of the EUC shear and baroclinicity in the eddy generation process is not clear from previous work. Philander (1976) has postulated that the EUC by itself (i.e., without surrounding westward flow) is stable, except perhaps for a barotropic instability in the Pacific during March and April when the EUC appears strongest due to the superposition of near-surface, annual cycle currents. Cox' (1980) model shows that zeros in the gradient of absolute vorticity (a necessary condition for barotropic instability on midlatitude β planes) are most prevalent during boreal summer and fall when the lateral shear between the EUC and the SECN is strongest. (As noted by Lukas 1987, and as shown in Fig. 6, even the overall mean zonal current distribution of the SEC and EUC in the central-eastern Pacific satisfies this condition.) On the basis of measurements made within 1° of the equator, both Lukas (1987) and Wilson and Leetmaa (1988) have suggested that the lateral shear on the north side of the EUC is a likely location for eddy energy production. Recent numerical studies by Philander et al. (1986) have identified the south side of the SEC as important in barotropic energy conversion, but not the EUC shear. They also suggest the importance of baroclinic instability near the equator, in agreement with the Cox (1980) and the Semtner and Holland (1980) models. Hansen and Paul's (1984) drifter data analysis indicates that baroclinic energy conversion is as important as barotropic energy conversion near the equator in the eastern Pacific, while Wilson and Leetmaa (1988) and Brady (1990) find only relatively minor baroclinic energy conversion within 1° of the equator in the eastern Pacific, and Weisberg and Weingartner (1988) find baroclinic energy conversion to be insignificant in the Atlantic.

The Philander et al. (1986) model emphasizes the seasonal nature of the instability due to the seasonally varying strengths of the equatorial surface currents. Observed equatorial current time series show the expected seasonal variability of the amplitude of the eddies and the amplitude of the horizontal Reynolds stress, in both the Pacific (Philander et al. 1985; Luther, Knox and Halpern, private communication 1988) and the Atlantic (Weisberg and Weingartner 1988). Early sea surface temperature (SST) observations also suggested a seasonal variability to the eddy amplitudes (Legeckis 1977; Legeckis et al. 1983), but SST is not a faithful indicator of the eddies since the horizontal gradients of SST depend in a complicated manner on the currents and air–sea heat fluxes. Despite the seasonal variability of the amplitude of the eddies, it is not known whether the annual cycle of the currents couples significantly with the eddies or simply acts to seasonally trigger (or dampen) the instabilities of the mean currents.

In an effort to elucidate the energetics of fluctuations in the upper equatorial Pacific, especially the possible local energy sources such as mean flow instabilities,

we have begun analyzing the repetitive sections of Doppler-measured currents and CTD-measured temperatures and densities which were obtained during the NORPAX Hawaii-to-Tahiti Shuttle Experiment of 1979–80, located between 150° and 158°W. The advantages of this dataset are that it contains latitude and depth information, it consists of a large number of sections with which means and seasonal variability may be defined, and it provides concurrent measurements of velocity, temperature, and density. The major disadvantage is that the data lack information on the frequency content of the nonannual fluctuations. For this we must rely on complementary information, from moored current meters for instance. Because the shipborne Acoustic Doppler Current Profiler (ADCP) measurements are still somewhat novel, this dataset is discussed in detail in section 2 and appendix A, where such questions as accuracy and aliasing are addressed. Furthermore, results that are on the edge of significance are presented at times in order to demonstrate the great potential of repetitive ADCP measurement programs. Significance levels will always be stated. The marginal results are of scientific interest; many of the less significant terms are small, and the rms errors of these terms establish upper bounds on the true sizes of the terms.

In section 3 of this paper, the eddy energy equations are derived with respect to the particular structure of the mean fields at the equator, and in light of the peculiarities of the available data. The multiple linear regression technique for defining the mean, annual cycle, and residual eddy variability of each field, and the procedures for estimating rms errors, are also discussed in section 3. Of the estimated quantities, the mean fields and eddy variances are presented first, in section 4, followed by estimates of the eddy energy equation terms, in section 5. The results presented in both sections 5 and 6, which addresses the seasonal variability of the eddy energetics, provide clear evidence of the intimate involvement of the EUC in the barotropic instability at these longitudes, while suggesting that baroclinic eddy energy production is not closely tied to the barotropic eddy energy production. It is also shown that conversion of energy from the annual cycle to the eddies is insignificant. Section 7 summarizes the energy equation estimates and collects the important inferences we have made from these estimates, while Section 8 presents a number of caveats and general comments.

2. Data

The NORPAX Shuttle Experiment took place from February 1979 through June 1980 (Wyrtki et al. 1981). The experiment included 15, approximately monthly, cruises on the nominal cruise track shown in Fig. 2. The ships collected CTD data every 1° of latitude or longitude along the track (Williams 1980–81), and occupied profiling current meter stations every 1° of latitude between 6°S and 10°N, with additional half-degree stations within 3° of the equator (Firing et al. 1981). Acoustic Doppler current profiles were collected continuously along the ship's track. The cruise track was traversed in alternate directions, so the shipboard data are sampled unevenly in time. In addition to these data, a set of three vector-averaging current meter moorings were maintained during the experiment at 0°40'N, 153°W; 0°40'S, 153°W; and 0°, 152°W (Knox and Halpern 1982).

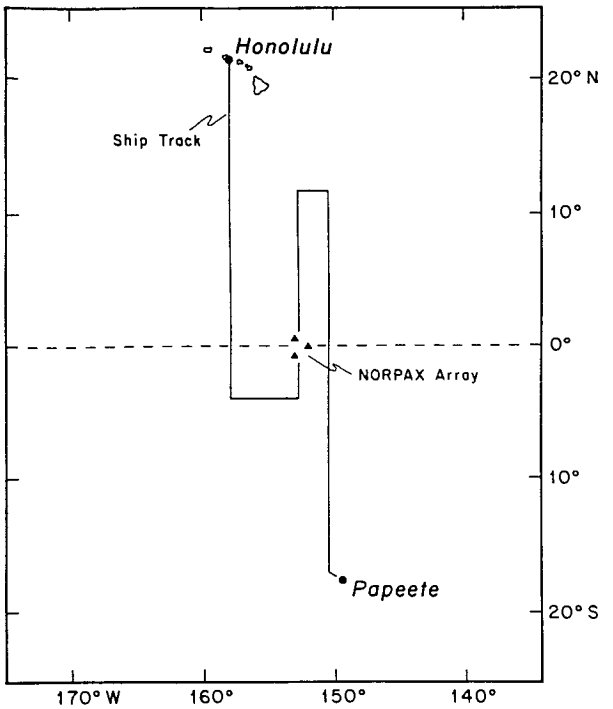

FIG. 2. The nominal cruise track during the Shuttle Experiment, and the concurrent mooring array. The present analysis averages data from all three longitudes together, and concentrates on the heavily sampled latitudes between 4°S and 10°N.

The ADCP data collection system was added to the Shuttle Experiment by Drs. Robert Knox, Lloyd Regier, and David Cutchin. It operated successfully on the last ten legs (legs 6 through 15). Of the 30 resulting sections, 3 are unusable: on leg 7 along 150°W most of the section is missing, on leg 8 along 158°W the deeper data is intermittent, and on leg 15 along 153°W the ship departed from the nominal north–south track and no CTD data was collected. Figure 3 shows in time–latitude format the location of the ADCP data recovered. The domain of the present analyses corresponds to the domain with the largest amount of high quality data, i.e., 10°N to 4°S, 26 to 117 m. Details of the ADCP data processing that yielded averaged absolute velocities for every 1° latitude along the ship track can be found in appendix A. A brief discussion of the CTD data and subsequent calculation of pressures can also be found in appendix A.

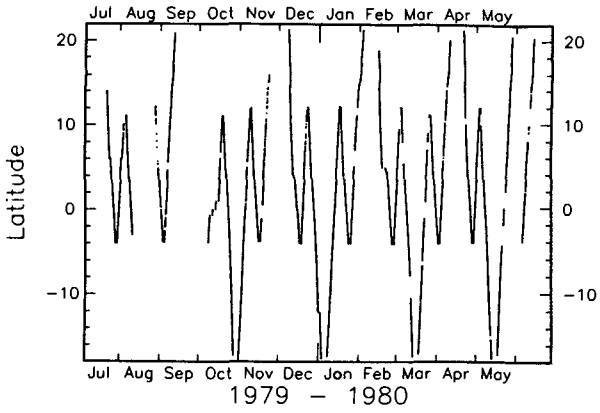

FIG. 3. The location of each 5 minute ADCP velocity profile in time and latitude. The profiles in the 27 usable sections between 4°S and 10°N were averaged into 1° latitude blocks before further analysis.

The ADCP data has unusual noise characteristics. Vertical shears are quite accurate, but absolute velocities are fairly noisy due to errors introduced by the heading and satellite fix datasets. Johnson et al. (1988) compared the ADCP data with concurrent but independent profiling current meter (PCM) data (Firing et al. 1981). They found the ADCP to have a rms noise level of (0.0018, 0.0016) s^{-1} for (eastward, northward) vertical shear over 13 m and about a quarter of that for 52 m shears. [Chereskin et al. (1987) found a comparable rms difference between 15 days of ADCP and VACM upper-ocean shears (over 20 m to 40 m) of about 0.002 s^{-1}.] Absolute ADCP velocities had rms noise levels of (14, 7) cm s^{-1} for (eastward, northward) velocity. The eastward noise is larger since it it more sensitive to heading errors.

The typical time interval between repeat sections in the Shuttle Experiment was too long to resolve the temporal scales of the variability observed; therefore, much of the variability is hopelessly aliased. Two issues arise from this: the distortion of the means and annual cycles by the higher frequencies, and the lack of information on the spectral content of the high frequencies.

There is no doubt that energetic high frequency fluctuations can bias estimates of mean quantities when discrete data sampling schemes are employed. Deterministic sinusoids at integer multiples of the Nyquist frequency in evenly sampled data can bias the mean of that data. Such biases are not mitigated by averaging over more data collected at the same sampling rate, nor can they be accounted for by error estimates based on stochastic noise assumptions. The only significant aliased deterministic signals in the present data are the tides, both the barotropic tides and those parts of the internal tides that are phase-locked to the gravitational forcing function. These signals are quite small compared to the observed means, and the irregular sampling of the shuttle data randomizes the tidal signals, reducing any bias effect on the mean (e.g., see Firing and Lukas 1985). Therefore we do not expect deterministic aliases of our mean quantities or of our annual cycles to be important.

Stochastic high frequency fluctuations also bias estimates of the means and annual cycles, but their effect tends to zero as more data is obtained at the original sampling rate, and the uncertainty in the mean estimate generated by their presence is readily calculated. Finally, although the ADCP data have been averaged over 1° latitude bins primarily in order to reduce navigational noise, the averaging also reduces the high frequency internal wave variability, although certainly not all internal waves are filtered.

The ADCP and CTD data could be analyzed to produce a frequency spectrum of energy, which we know would be contaminated by the aliasing of high frequencies (in this case, any frequency greater than about 1 cycle/month). Luther and Harrison (1984) showed with meteorological time series that infrequent numbers of samples in each month can easily result in overwhelming amounts of high frequency energy being added to the low frequency spectrum. This means that with only 2 or 3 observations per month at each location we have no a priori knowledge regarding which frequencies contribute to the variability in the ADCP and CTD data at periods shorter than one-half year. This lack of spectral information restricts the kinds of analyses that can be accomplished; for instance, evaluation of wave action density and its conservation is prohibited. But for this study, where the intent is to determine the quality and structure of eddy–mean flow interactions, the lack of spectral information is secondary to the question of whether the variability interacts with the mean flow at all. If significant interactions are found, we must bring in complementary measurements to determine spectral content; otherwise, the spectral content will remain a mystery until more densely sampled data is collected. But the issue of whether any eddy–mean flow interaction occurs can be determined from the ADCP and CTD data, irrespective of the scrambled frequency content of the variability.

3. Energy equations, analysis procedures, and error estimation

a. Energy equations

Each variable is assumed to have a time-independent (mean) part, a slowly-varying part, and a rapidly-varying part; and it is assumed that the temporal scales of these parts do not overlap:

$$u = \bar{U}(x, y, z) + \tilde{U}(x, y, z, t) + U^*(x, y, z, t),$$

$$v = \bar{V}(x, y, z) + \tilde{V}(x, y, z, t) + V^*(x, y, z, t),$$

$$w = \bar{W}(x, y, z) + \tilde{W}(x, y, z, t) + W^*(x, y, z, t),$$

$$T = T_0(z) + \bar{T}(x, y, z) + \tilde{T}(x, y, z, t) + T^*(x, y, z, t),$$

$$\rho = \rho_0(z) + \bar{\rho}(x, y, z) + \tilde{\rho}(x, y, z, t) + \rho^*(x, y, z, t),$$

$$P = P_0(z) + \bar{P}(x, y, z) + \tilde{P}(x, y, z, t) + P^*(x, y, z, t), \quad (3.1)$$

where $(\bar{\ })$ means an average over the entire time period of observation, $(^*)$ mean a high-frequency residual, and $(\tilde{\ })$ denotes variability on time scales short with respect to the time period of observation but long with respect to the high-frequency residuals. In the present case, the mean and the low frequency variability are estimated with a multiple linear regression discussed below. The high-frequency residuals result from subtracting the mean and low frequency variability from the original data. In addition, a constant, ρ_*, is defined as the average or volume integral of density. Cartesian coordinates have been defined in the usual sense. Note that by definition $\overline{(\tilde{X}_i)} = \overline{(X_i^*)} = 0$ where X_i is any variable, and also that $\overline{\tilde{X}_i X_j^*} = 0$.

Assuming negligible viscosity and no external forcing, the equation for the rate of change (over very long time scales) of the kinetic energy of the high-frequency variability is as follows:

$$\frac{\partial}{\partial t}\overline{\mathrm{KE}^*} = -\overline{U_k}\frac{\partial}{\partial x_k}\overline{\mathrm{KE}^*} - \overline{\tilde{U}_k\frac{\partial}{\partial x_k}\widetilde{\mathrm{KE}^*}} - \overline{U_k^*\frac{\partial}{\partial x_k}\mathrm{KE}^*} - \overline{U_k^*\frac{\partial}{\partial x_k}P^*} - g\overline{W^*\rho^*} - \rho_*\overline{U_i^*U_k^*}\frac{\partial}{\partial x_k}\overline{U_i} - \rho_*\overline{U_i^*\tilde{U}_k^*}\frac{\partial}{\partial x_k}\tilde{U}_i, \quad (3.2)$$

where

$$\mathrm{KE}^* \equiv \frac{1}{2}\rho_*(U^{*2} + V^{*2} + W^{*2})$$

and the subscripts i and k are 1, 2, or 3 referring to the 3 velocity components (u, v, w) or directions (x, y, z), and subscripts in any term imply summation over that subscript. The continuity equation, $\partial U_k/\partial x_k = 0$, has not been added to (3.2), as is usual to commute U_k and $\partial/\partial x_k$ in the various terms. In general, the data used here do not sample zonal and meridional gradients simultaneously, so that continuity holds only in the statistical mean. Therefore, adding continuity to a term introduces oceanic noise as well as additional instrumental noise. The added noise can be substantial, as will be seen in section 5c.

The time derivative implies temporal variation of the mean over time scales greater than the period of observation. The first three terms of the right hand side of (3.2) represent advection of KE* by mean, low-frequency, and high-frequency flows, respectively. The fourth term represents diffusion by fluctuating pressure gradients. The fifth term is the gain of energy through fluctuating buoyancy forces. The sixth term is production of fluctuation energy by the mean flow working on the fluctuation Reynolds stresses. And the seventh term is production of fluctuation energy by the low-frequency flow working on the fluctuation Reynolds stresses. If $\overline{\mathrm{KE}^*}$ doesn't change over very long time scales, then any imbalance of the right hand side of (3.2) implies that external forces or dissipation are important in the energy balance.

It is readily argued, by a scaling analysis of equatorial mean and low-frequency currents, that over half of the terms in the energy production tensors of (3.2) are much weaker than at least one other term in the same tensor, e.g.,

$$\left|-\rho_*\overline{V^*U^*}\frac{\partial}{\partial x}\bar{V}\right| \ll \left|-\rho_*\overline{U^*V^*}\frac{\partial}{\partial y}\bar{U}\right|,$$

since

$$\left|\frac{\partial}{\partial x}\bar{V}\right| \ll \left|\frac{\partial}{\partial y}\bar{U}\right|.$$

However, even after discarding the weaker terms, all three residual velocities as well as derivatives in all three directions are present in the remaining source terms; none of these remaining terms can be ruled out a priori, although it can be argued that the terms dependent on $\overline{U^*V^*}$ and $\widetilde{U^*V^*}$ are likely to be the most important in their respective tensors.

In order to improve the statistical reliability of the calculations performed later in this paper, all the NORPAX shuttle sections have been lumped together, thus ignoring zonal variability. This is justified since Johnson et al. (1988), Wyrtki and Kilonsky (1984), Firing and Lukas (1985), and Lukas and Firing (1985) all conclude that the means from each longitudinal section are statistically indistinguishable. Also, it is known that the annual cycle of thermocline temperature in the study region has only a small westward phase lag, of no more than 1°–2° per degree of longitude (Meyers 1979). Similar results obtained for the annual cycle of zonal velocity extracted from the ADCP data at each longitude, and for zonal velocity from the Tropic Heat moorings along the equator from 110° to 140°W (Luther, Knox and Halpern, private communication 1988). Therefore, the annual cycle can be estimated from the data asssuming no zonal change from 150° to 158°W without incurring much error.

Neglecting zonal variations eliminates all terms in (3.2) having zonal derivatives. Vertical velocities are unavailable as well. Although we do not directly estimate terms containing vertical velocity or zonal gradients, some of these terms may be important, as discussed in section 7e.

The resultant incomplete kinetic energy equation that is examined in this study is as follows:

$$\frac{\partial}{\partial t}\overline{\mathrm{KE}^*} = -\bar{V}\frac{\partial}{\partial y}\overline{\mathrm{KE}^*} - \overline{\tilde{V}\frac{\partial}{\partial y}\widetilde{\mathrm{KE}^*}} - \overline{V^*\frac{\partial}{\partial y}\mathrm{KE}^*}$$
$$- \overline{V^*\frac{\partial}{\partial y}P^*} - \rho_*\overline{U^*V^*}\frac{\partial}{\partial y}\bar{U} - \rho_*\overline{V^*V^*}\frac{\partial}{\partial y}\bar{V}$$
$$- \rho_*\overline{U^*\widetilde{V}^*}\frac{\partial}{\partial y}\tilde{U} - \rho_*\overline{V^*\widetilde{V}^*}\frac{\partial}{\partial y}\tilde{V}. \quad (3.3)$$

An additional approximation that is made, which leads to little error, is the neglect of W^{*2} in the estimation of KE*.

The potential energy conservation equation can be derived following similar lines of argument as for the kinetic energy equation, and is as follows:

$$\frac{\partial}{\partial t}\overline{\mathrm{PE}^*} = -C\overline{U_k}\frac{\partial}{\partial x_k}\overline{\tfrac{1}{2}\rho^{*2}} - C\overline{\tilde{U}_k\frac{\partial}{\partial x_k}\tfrac{1}{2}\widetilde{\rho^{*2}}}$$
$$- C\overline{U_k^*\frac{\partial}{\partial x_k}\tfrac{1}{2}\rho^{*2}} + g\overline{W^*\rho^*}$$
$$- C\overline{\rho^*U_j^*}\frac{\partial}{\partial x_j}\bar{\rho} - C\overline{\rho^*\widetilde{U}_k^*}\frac{\partial}{\partial x_k}\tilde{\rho}, \quad (3.4)$$

where

$$\mathrm{PE}^* \equiv \tfrac{1}{2}C\rho^{*2},$$
$$C = -\frac{g}{\frac{\partial}{\partial z}(\rho_0 + \bar{\rho})}.$$

Note that while k refers to the three directions and velocity components, j refers only to the horizontal directions and velocity components, since the vertical eddy potential energy production is absorbed into the term $g\overline{W^*\rho^*}$ due to the inclusion of $\bar{\rho}$ in the definition of PE*. The definition of PE* in (3.4) is derived from the traditional definition (Reid et al. 1981),

$$\mathrm{PE}^* = \tfrac{1}{2}(\rho_0 + \bar{\rho})N^2\zeta^{*2},$$

(for N the buoyancy frequency) by approximating the local isopycnal displacement, ζ^*, with

$$\zeta^* = \rho^* \Big/ \frac{\partial}{\partial z}(\rho_0 + \bar{\rho}).$$

This produces a form which is more useful computationally. However, since the approximation for ζ^* results from a one term Taylor series expansion for ρ^* in terms of ζ, it therefore requires the assumption that ζ is small relative to the vertical scales of the mean stratification. This assumption is valid in the pycnocline, but is somewhat strained in the mixed layer, as will be seen in section 5c and in Fig. 20.

Further, PE* has been defined relative to the mean stratification. That is, the rest state in which no eddy potential energy is present is taken to be the mean density structure, $[\rho_0(z) + \bar{\rho}(x, y, z)]$. This differs from the usual definition of available potential energy, in which the rest state is that state of minimum total potential energy achieved by redistributing the water masses (without mixing) until the isopycnals are everywhere level (Reid et al. 1981). This latter rest stratification is given by $\rho_0(z)$ if compression effects are neglected. Since $\bar{\rho}$ is a strong, nonuniform function of latitude here, the minimum energy rest state is not representative of the total mean stratification at any location. Therefore, an accurate representation of PE* in the various regions of the study area requires the inclusion of $\bar{\rho}$ in the definition of potential energy.

Since $\bar{\rho}$ is included in the definition of PE*, the quantity C in (3.4) does not generally commute with $\partial/\partial x_k$. Therefore the mean advection of PE* on the right of (3.4) cannot be expressed as the advection of a conservative quantity, as for KE* in (3.2), without the inclusion of a "correction term" dealing with the gradients of $\bar{\rho}$:

$$-C\overline{U_k}\frac{\partial}{\partial x_k}\overline{\tfrac{1}{2}\rho^{*2}} = -\overline{U_k}\frac{\partial}{\partial x_k}\overline{\mathrm{PE}^*} + \tfrac{1}{2}\overline{\rho^{*2}U_k}\frac{\partial}{\partial x_k}C$$

where the last is the correction term. Previous investigations have specifically neglected the correction term (e.g., Szabo and Weatherly 1979) or kept it (e.g., Dewar and Bane 1985); but for the present data it can be shown that all three of the above terms are of similar size, so that both components of PE* advection must be retained. In short, PE* does not advect conservatively. Splitting the advection of PE* into conservative advection and correction components does not result in much useful physical information. Therefore, we will continue with the non-conservative advection terms as written in (3.4).

The first three terms on the right-hand side of (3.4) represent the gain in PE* through the effects of non-conservative advection by the mean, the low-frequency, and the high-frequency flows, respectively. The fourth term in (3.4) is the gain in $\overline{\mathrm{PE}^*}$ from fluctuating buoyancy forces. The conversion of mean and low-frequency PE to high-frequency PE are the fifth and sixth terms, respectively. As for kinetic energy, terms containing zonal gradients or vertical velocities are neglected, leaving

$$\frac{\partial}{\partial t}\overline{\mathrm{PE}^*} = -C\bar{V}\frac{\partial}{\partial y}\overline{\tfrac{1}{2}\rho^{*2}} - C\overline{\tilde{V}\frac{\partial}{\partial y}\tfrac{1}{2}\widetilde{\rho^{*2}}}$$
$$- CV^*\frac{\partial}{\partial y}\tfrac{1}{2}\rho^{*2} - C\overline{\rho^*V^*}\frac{\partial}{\partial y}\bar{\rho} - C\overline{\rho^*\widetilde{V}^*}\frac{\partial}{\partial y}\tilde{\rho}. \quad (3.5)$$

b. *Analysis procedures*

The mean, low-frequency, and high-frequency fields are estimated using a multiple linear regression (MLR).

The MLR fits each variable on the left-hand side of (3.1) with a function of the form

$$X(y, z, t) = X_1(y, z) + X_2(y, z)\cos(\omega t) + X_3(y, z)\sin(\omega t) + X_4(y, z)\cos(2\omega t) + X_5(y, z)\sin(2\omega t) + R(y, z, t) \quad (3.6)$$

where ω is one cycle per year. The fit occurs separately at each latitude and depth, and minimizes $R(y, z, t)$ over time in a least squares sense. The mean field in (3.1) is then X_1, the low-frequency field is the sum of 1 and 2 cpy sinusoids, and the high-frequency residual field is R. For T, ρ and P, the MLR mean is divided into $X_0(z)$, the meridional average of $X_1(y, z)$, and $\bar{X}(y, z)$, the remainder containing the mean latitudinal structure.

No trend is contained in the MLR, since in general a trend is not orthogonal to the 1 cpy sinusoid, and for time series shorter than 13 months, estimating a trend and annual cycle together results in poor estimates of both (Firing and Lukas 1985). For the present 11 month series the nonorthogonality is severe. In any case, the trend in 1979–80, representing interannual variability, was small relative to the annual cycle for both velocity on the equator (see Fig. 1) and temperature in the central Pacific (e.g. Kessler and Taft 1987). The 2 cpy sinusoids are included since they are an important part of the annual cycle at some latitudes. This is seen in Fig. 4, which shows total zonal velocity (i.e., before the MLR) averaged over the depths 26 to 117 m and over 2 month blocks to suppress the highest frequencies. The relative insignificance of any trend is also apparent: any trend would show up as a jump in velocity between the end of time period C (8 June 1980) and the beginning of A (27 July 1979).

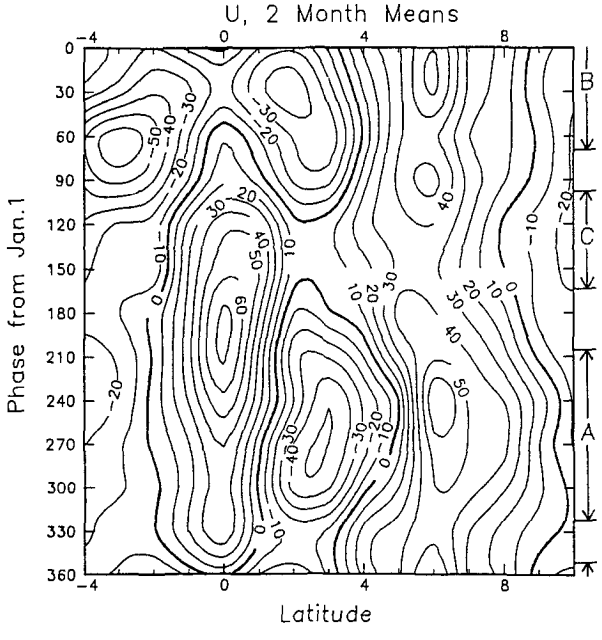

FIG. 4. The vertically averaged zonal velocity as a function of latitude and time (plotted here as phase, 360° = 1 year). Points exist every 1° in latitude and 30° in phase. The ADCP velocities are smoothed with a 2-month block average to suppress the high frequencies. Units are cm s^{-1}. Note that the major currents vary strongly throughout the year. Along the right axis are noted the three time periods defined in section 6. The year of data begins with time period A and ends at the end of period C.

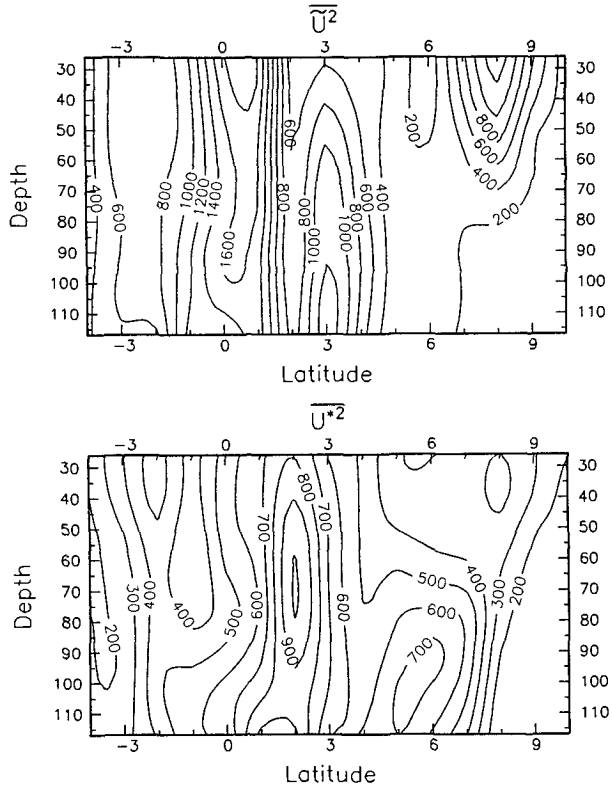

FIG. 5. The zonal velocity variance of the low-frequency field, $\overline{U}^2$, and the high frequency residuals, U^{*2}. Units are $cm^2\ s^{-2}$. The two fields have very different structures, implying different sources of variability.

The residual sections are independent in time; their time-lagged covariance function falls to zero or less at even the shortest lags observed (see appendix B). Therefore no weighting is needed in the MLR to mitigate correlation among the data. Whether a weighting scheme should be devised to account for the irregular sampling is debatable, and none has been attempted.

The MLR removed a substantial amount of low-frequency variance. For example, low-frequency zonal velocity accounts for 44% of the total zonal velocity variance. Figure 5 shows the variances of the zonal low-frequency and high-frequency fields. Note that the greatest variability is found in different locations for the different time scales.

Distinct components (i.e. different frequency bands) of the MLR for each oceanic variable at a given point are exactly orthogonal over the time series [e.g.,

$\overline{U^*(y, z, t)\tilde{U}(y, z, t)} = 0$]. However, the presence of occasional holes in the data disturbs such orthogonality between components of different oceanic variables or for the same variable at two locations, since in such cases the original time series do not necessarily contain the same time points. In the worst case, there is a correlation of 0.13 between supposedly orthogonal regression function components; all other correlations are less than 0.09.

In this paper spatial derivatives are evaluated with two-point finite differences. This reduces the dimension of a gradient field by one point in the direction of the derivative. When fields of gradients are multiplied by other quantities, those quantities are first filtered with a two-point running mean to match both the field size and the spatial averaging scales with the gradient. Contoured plots are produced by a computer program that exactly fits a smooth surface to the data points using a combination of cubic splines and the Laplace equation. Splines are weighted to emphasize curvyness over pointyness, but changing this weighting does not alter the plots shown to any degree except in the noisiest, spatially-aliased scales.

c. *Error estimation*

Errors due to stochastic high-frequency variability are estimated for all the quantities presented. Formulas are derived in detail in appendix B. The error bars presented are root-mean-square errors. To the extent that the variability of a quantity is relatively small has a Gaussian distribution, two such rms errors in either direction represent 95% confidence limits. The major assumption used to estimate the rms errors is that the data are joint-normally distributed. This assumption is examined further in appendix B. The residual high-frequency sections are considered independent (see 3b above), and the degrees of freedom (DOFs) available are reduced by five to account for those lost to the MLR fit of the mean and low-frequency fields above. It is important to note that the rms errors apply only to the uncertainty with which a given quantity is observed by the present datasets for the year sampled. They contain no information regarding the interannual stability or stationarity of that quantity.

Later in the paper, integrals over depth and latitude will be calculated to obtain volume estimates of energy production rates and other quantities. The number of independent points in a (y, z) section has been estimated by computing the spatial correlations of the basic variables, U, V, etc. On the average, there are about 2 independent points in the vertical and about 4.5 in latitude, for a total of 9 over an entire section. For functions of the data more complicated than means (such as variances, etc.), there will be more independent points in the (y, z) domain than is estimated by the spatial correlation functions of the basic variables, since the complicated functions tend to have shorter correlation scales. But for simplicity, we use the above average estimate of independent points and note that this approximation results in error estimates that are slightly larger than they should be for all but the simplest functions of the data.

4. Mean fields and fluctuation variances and covariances

a. *Mean fields*

To familiarize the reader with the area of the ocean studied, and as a basis for understanding later results, the mean fields observed during the study period are presented first. Figure 6 shows the mean zonal velocity, $\bar{U}(y, z)$ of (3.1), as determined by the MLR fit (3.6). The strong zonal currents of the region are clearly seen; the eastward flowing EUC underlies the westward SEC at the equator, the eastward NECC appears from 4° to 9°N, and the edge of the westward North Equatorial Current (NEC) appears north of 9°N. The rms errors associated with the means are small relative to the means. Notice that due to the limited depth penetration of the instrument we have not observed the core of the

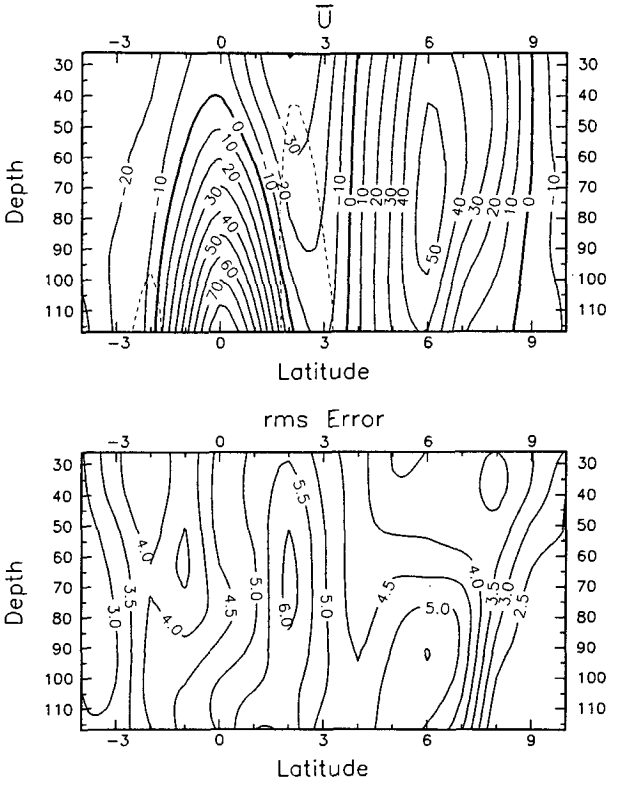

FIG. 6. The mean zonal velocity from a multiple linear regression using the 27 sections of data, with the rms errors. Units are cm s^{-1}. Note the strong SEC, EUC, and NECC and their large meridional shears, as is also seen in Fig. 4. All the currents are highly significant. The dashed lines are zero contours for the gradient of absolute vorticity, $\beta - \bar{U}_{yy}$.

EUC. Concurrent profiling current meter (PCM) data show the mean core velocity to be 100 cm s^{-1} at about 135 m depth (Lukas and Firing 1984). Similarly, the topmost 26 m are not observed as noted in appendix A. The mean zonal velocity is in very close geostrophic balance with the mean pressure gradient relative to a 300–500 m average reference level (Lukas and Firing 1984; Johnson et al. 1988).

The mean meridional flow shown in Fig. 7 is much smaller than the zonal flows; hence the observational error is proportionately larger. Still, the major features of the mean are significant. There is convergence in the upper EUC between 3°S and 3°N, the larger features of which are statistically significant at 2 rms errors or better. The large divergence near the surface at 1°–4°N is also significant, although the rms errors indicate that the location of the zero velocity contour is not well known. The strong northward current from 3° to 6°N is a robust, significant feature present at all three longitudes of this dataset. A similar current is seen in the numerical model of Philander et al. (1986, 1987) and has been observed and modeled in the Atlantic (Richardson and Philander 1987). Note that there is no southward flow in the thermocline at the NECC, contrary to the expectations of Wyrtki and Kilonsky

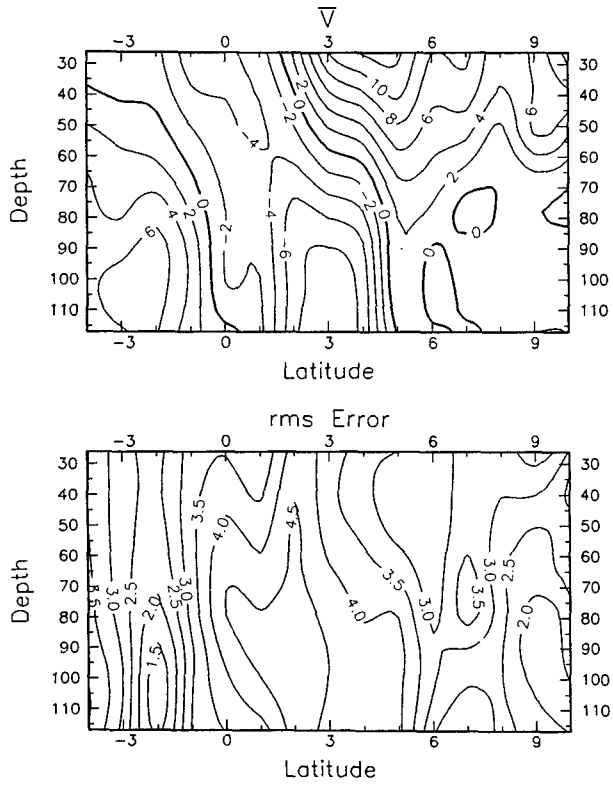

FIG. 7. As in Fig. 6, but for meridional velocity. Note the convergence on the equator below about 50 m depth, and the generally poleward near-surface flow. The major features are all significant at 95% confidence (see text).

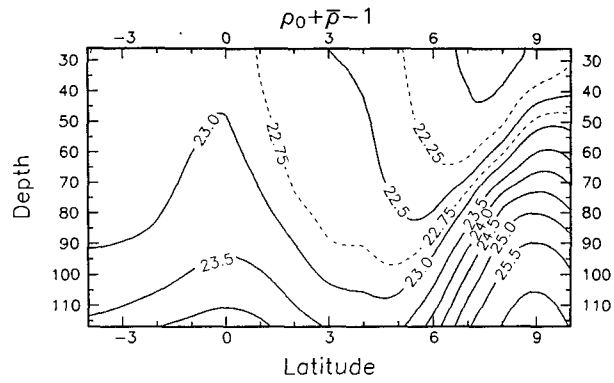

FIG. 8. The mean potential density (σ_θ), in 10^{-3} g cm^{-3}. The mean density implies a pressure field that is in close geostrophic balance with the mean zonal velocity (Fig. 6).

(1984); the errors of the mean are large enough that the true flow could be of either sign, but is apparently not of the same magnitude as the southward flow centered at 110 m at 3°N. In agreement with these observations, the numerical model of Philander et al. (1987) exhibits meridional circulation that is tightly confined (0°–6°N) north of the equator, at least during part of the year, in the central-eastern Pacific.

The mean density field is shown in Fig. 8. Note that only north of 7°N does the study region include the entire pycnocline. The density field is roughly symmetric within 2° of the equator, where the temperature field (not shown) is not, due to the presence of higher salinities south of the equator (Wyrtki and Kilonsky 1984). The equatorial front does not appear in Fig. 8 as the sharp front sometimes observed in satellite images (e.g., Legekis et al. 1983). The front does not occupy the same position at all times, and so is smeared in the mean, but is generally indicated by a weak maximum in $\partial\overline{\rho}/\partial y$ at 3°–6°N. The temperature difference across the front is weaker at this longitude than further east; the temperature difference from 0° to 6°N at 30 m depth is 1.3°C here, but is about 2°C in Hansen and Paul's (1984) study between 100° and 130°W. The gradient is also a strong function of depth.

b. *Variances*

Figures 5 and 9 show the variances of the zonal and meridional high-frequency velocity residuals, U^* and V^*, respectively. The rms errors of these estimates are 30% of the estimates themselves. Note that the high-frequency variances are much larger than the estimated measurement errors of the ADCP, which are 193 and 55 cm^2 s^{-2} for U and V, respectively (Johnson et al. 1988). Some of the original variance of the data has been removed in the annual cycle (see Fig. 5), mostly from U. This low-frequency variance has a different latitudinal structure than the high-frequency variance. The high-frequency variances have significant peaks at

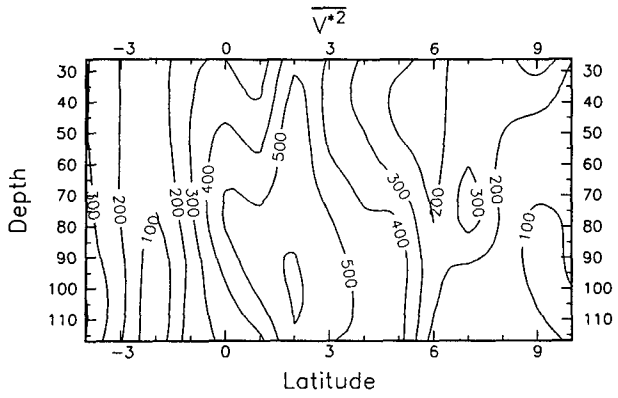

FIG. 9. The variance of the high-frequency residuals of meridional velocity, $\overline{V^{*2}}$, in cm^2 s^{-2}.

2°N for both U^* and V^*, and at 5° to 6°N for U^*. The latitudinal structure of the variance peaks cannot be easily explained by ambient high-frequency internal waves or by equatorially trapped internal waves; the former should have a uniform variation of energy with latitude (Munk 1980; Fu 1981; Eriksen 1980) while the latter do not have patterns of energy which are asymmetric about the equator unless a sum of many phase-locked modes is invoked. Equatorial Kelvin waves are observed in the area (Knox and Halpern 1982), but the expected zonal velocity signature of a maximum at the equator decaying poleward is not apparent in Fig. 5. This is not surprising since the Kelvin waves are relatively weak in the top 100 m, being strongest at the 150-m and 250-m instrument depths, well below the ADCP observation depths (see also McPhaden and Taft 1988).

Near the equator the frequency content of the high-frequency fields can be found from the concurrent observations from the NORPAX moorings. Figure 10 shows the variance preserving spectra of both components of horizontal velocity at 100 m depth averaged over the two moorings for which complete records are available. The nominal mooring locations are 0°40′N, 153°W; and 0°, 152°W (Knox and Halpern 1982). The areas under the curves of Fig. 10 are proportional to variance or energy. Most of the velocity variance is in the annual cycle and in the 10–30 day band, with a smaller contribution from the tides and other fluctuations at periods less than 8 days. The annual cycle cannot be responsible for the observed ADCP high-frequency variance (in Figs. 5 and 9) as it is segregated into the low-frequency field. The internal tides should be heavily filtered by the 1-deg latitude spatial filtering of the ADCP data since they have horizontal wavelengths on the order of 100 km (Hendry 1977; Wunsch 1975). Also, the internal tides are characterized by equal U and V variances and by weak dependence of their variances on latitude, so they are unlikely to be responsible for the observed high-frequency variability. Therefore, we conclude that the ADCP high frequencies are dominated by the 4–60 day frequency band near the equator. The ADCP data is coherent over 2° of latitude, as determined by calculation of spatial correlation functions, so the variance peak at 2°N should also be dominated by the 4–60 day variability.

To the north in the NECC no direct measurement of frequency content is available for the NORPAX year. However, the annual cycle has been removed and the high-frequency internal gravity waves are subject to spatial filtering as above, so we expect the ADCP high-frequency field to be dominated by variability in the 2–100 day band. At latitudes of the NECC one expects the velocity spectra to have prominent inertial peaks at 3–7 day periods. Halpern (1979) has observed such a peak at 8°27′N, 150°45′W. Inertial oscillations, however, are nearly circularly polarized and should have roughly equal U and V variance; therefore inertial oscillations cannot explain the presence of a U^* variance peak at 6°N without a concomitant V^* peak.

c. Covariances

The high-frequency flow interacts with the mean flow through the high-frequency covariances. Figure 11 shows the covariance, $\overline{U^*V^*}$, along with its errors. The dominant features are a broad maximum at 0°–

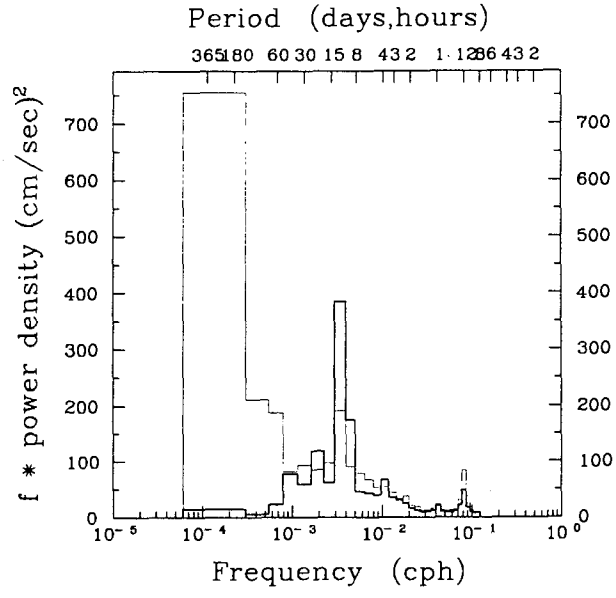

FIG. 10. The average of the variance preserving spectra of currents from 100 m depth from the moorings at 0°, 152°W and 0°40′N, 153°W. The areas under the curves are proportional to the original variances in a given frequency band. U, the light line, is dominated by annual scale variance, with a secondary contribution from the 4–60 day band. V, the heavy line, is dominated by the 4–60 day band. The tidal variance is small. The analysis attempts to concentrate on the 4–60 day band by eliminating the means and the annual scale variability using a multiple linear regression (section 3b). This in effect removes the lowest frequency block shown (1 and 2 cpy).

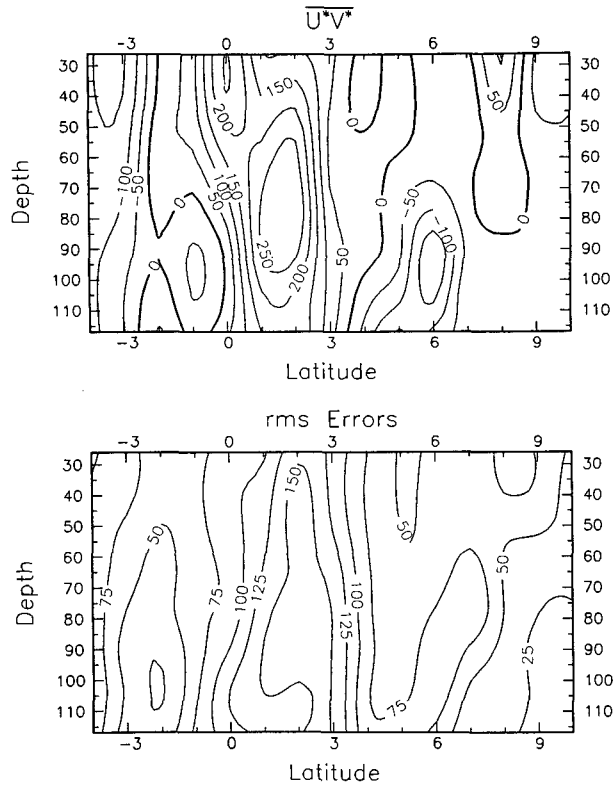

FIG. 11. The residual covariance $\overline{U^*V^*}$, with rms errors. Units are $cm^2 s^{-2}$. Note the strong positive values at 0° to 3°N, with negative values south of 2°S and subsurface at 5° to 7°N. The maxima are significant at 2 rms errors.

3°N associated with the velocity variance peaks there, a smaller maximum in the NECC thermocline corresponding to the second zonal velocity variance peak, and a surface intensified peak at the southern edge of the region. These three maxima are significantly different from zero at around 2 rms errors, or roughly 95% confidence. The positive values between 0° and 3°N correspond to momentum fluxes that are down the mean gradient of zonal velocity (see Fig. 6). The magnitudes of $\overline{U^*V^*}$ are comparable to those found near the surface in western boundary currents. For example, Szabo and Weatherly (1979) found values of around 500 $cm^2 s^{-2}$ in the Kuroshio Extension. The ADCP estimates of $\overline{U^*V^*}$ compare well with the calculations of Lukas (1987) using the moored current meter (MCM) data. Table 1 compares his estimates with ADCP estimates interpolated to the latitudes of the moorings where necessary. Note that the MCM records contain an additional four months of data, April through July 1979. There are no differences between the datasets greater than one rms error. Only two of the ADCP values and one of the MCM values are different from zero at 95% confidence, but the general pattern of higher values at shallow depths and to the north are apparent in both datasets. In addition, Lukas found integral time scales of 3–5 days for the MCM U^*V^* time series, implying periods of 19–31 days. This roughly corresponds to the most energetic part of the 8–60 day band of eddy variability in Fig. 10.

Figure 12 shows the density fluxes, $\overline{U^*\rho^*}$ and $\overline{V^*\rho^*}$. The largest maxima appear at 0° to 1°N and at 5° to 8°N. At 0° to 1°N, $\overline{V^*\rho^*}$ is significant at 95% confidence, but $\overline{U^*\rho^*}$ is not quite. At 5° to 8°N, $\overline{U^*\rho^*}$ is significant at nearly two rms errors but $\overline{V^*\rho^*}$ is only one rms error away from zero. Positive (negative) values of $\overline{U^*\rho^*}$ imply upgradient (downgradient) fluxes, assuming the pycnocline slopes up towards the east at all latitudes. Hence there is zonal downgradient flux in the NECC and upgradient flux in the EUC. The negative values of $\overline{V^*\rho^*}$ in the NECC imply meridional downgradient flux (see Fig. 8), while negative values of $\overline{V^*\rho^*}$ at 0° to 1°N imply upgradient flux. Bryden and Brady (1989) found negative values of $\overline{V^*\rho^*}$ at 50 and 150 m with the MCM data from 0°, 152°W and 40′N, 153°W, but not at 100 m as in Fig. 12b. This discrepancy may be due to the substantial differences between the datasets in their spatial and temporal coverages. A more detailed comparison of ADCP and MCM density fluxes will appear in a subsequent paper.

5. Mean fluctuation energetics

a. *Kinetic energy production*

The data clearly demonstrate the local production of eddy kinetic energy during the NORPAX shuttle. The largest of the eddy kinetic energy production terms that we can estimate [see (3.3)] is the quantity $-\rho_* \overline{U^*V^*}(\partial\bar{U}/\partial y)$ shown in Fig. 13. The major feature is a large peak of eddy energy production at 1° to 2°N, which corresponds to maxima in zonal and me-

TABLE 1. Estimates of $\overline{U^*V^*}$ derived from NORPAX moored current meter measurements by Lukas (1987), compared with ADCP estimates interpolated to the same positions. Rms errors are shown. Units are $cm^2 s^{-2}$.

	ADCP			MCM (Lukas 1987)		
	0°40′S	0°	0°40′N	0°40′S	0°	0°40′N
50 m	110 ± 70	204 ± 80	191 ± 90	—	140 ± 60	—
100 m	−32 ± 80	13 ± 100	136 ± 130	7 ± 42	50 ± 34	61 ± 45

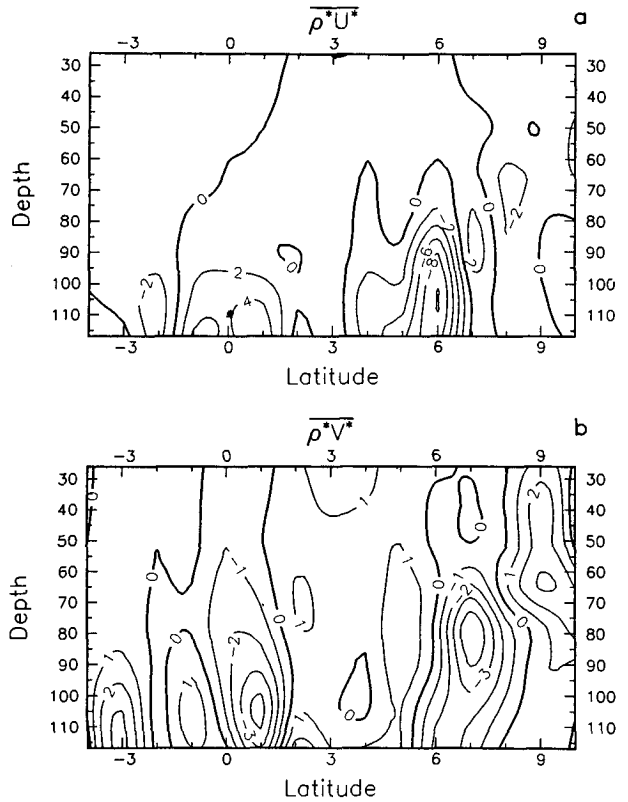

FIG. 12. The residual covariances of (a) $\overline{\rho^*U^*}$, and (b) $\overline{\rho^*V^*}$. Units are g cm^{-2} s^{-1}. If the pycnocline slopes up toward the east, the negative values of $\overline{\rho^*U^*}$ in the NECC correspond to downgradient density fluxes. Referring to Fig. 8, note the downgradient flux of $\overline{\rho^*V^*}$ in the thermocline of the NECC (6° to 8°N) but the upgradient fluxes in the EUC (2°S to 2°N).

ridional eddy velocity variability at the same location (see Figs. 5 and 9). The eddy energy production peak is significant at about 1.8 rms errors and will be considered, as usual, an indication of barotropic instability of the mean zonal currents. The maximum values occur below 50 m and large values apparently extend deeper than 117 m, showing that the lateral shear of the EUC is important in the eddy energy production at these longitudes. In the Atlantic Ocean Weisberg and Weingartner (1988) have found barotropic eddy energy production to be dominated by $-\rho_* \overline{U^*V^*}(\partial \bar{U}/\partial y)$ in the near-surface cyclonic shear of the SECN (the EUC is apparently uninvolved). The maximum near-surface values of 340×10^{-6} erg cm^{-3} s^{-1} (34 μW m^{-3}) in Fig. 13 are much less than the nearly 500 μW m^{-3} found further to the east by Hansen and Paul (1984, Fig. 8), but their estimate was obtained from drifter data spanning only that part of 1979 (summer–fall) during which the eddies were most energetic. We will further compare our results with those of Hansen and Paul in section 6, where the energetics over shorter time intervals will be examined. For now, both the present figure and Hansen and Paul's show maximum values for this term of eddy energy production occurring between 0° and 2°N. Outside of the 0°–2°N region our energy production values are quite weak, perhaps hinting at eddy energy loss regions on either side of the strong production region, and an eddy energy gain/loss dipole at 6°N in the thermocline. The average of this component of eddy kinetic energy production between 1°S and 3°N (which roughly encompasses the energy production region) is 234×10^{-6} erg cm^{-3} s^{-1}.

The other estimable barotropic mean to eddy kinetic energy production term, $-\rho_* \overline{V^*V^*}(\partial \bar{V}/\partial y)$ in Fig. 14, shows only weak eddy energy production in the region of the EUC, with slightly stronger loss regions to the north and near-surface. The energy gain regions are only 1.2 rms errors from zero, while the two peaks in the loss region are significant at about 2 rms errors. The average eddy energy gain between 1°S and 3°N

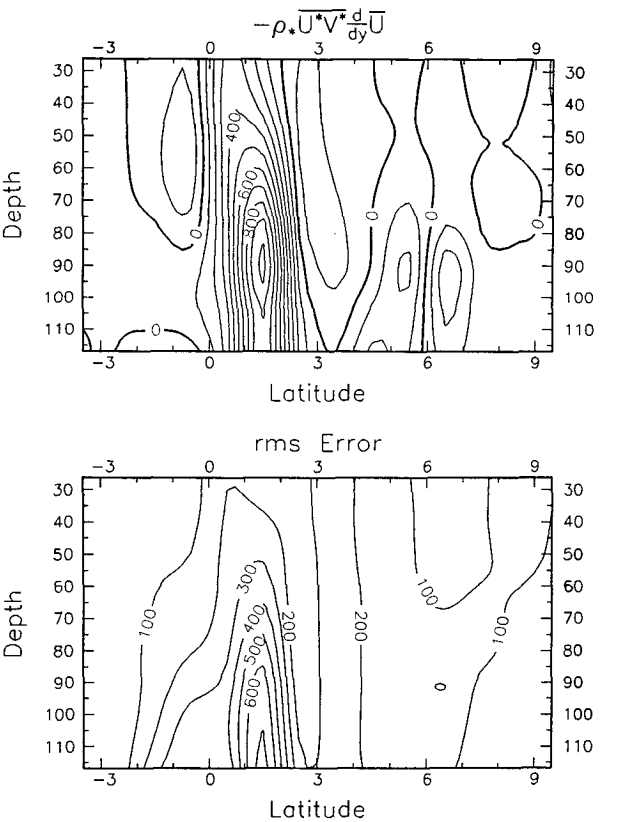

FIG. 13. The mean-to-eddy kinetic energy conversion term $-\rho_* \overline{U^*V^*}(\partial \bar{U}/\partial y)$, with rms errors. Units are 10^{-6} erg cm^{-3} s^{-1}. This is the largest component of the barotropic energy conversion. The strong peak of eddy energy gain at 1° to 2°N is significant at 1.8 rms errors, and corresponds to the U^{*2} and V^{*2} peaks in Figs. 5 and 9 and to the $\overline{U^*V^*}$ peak in Fig. 11. Note that the values in the NECC are small, with no net effect. (In this and subsequent figures, the derivatives that appear at the tops of the figures imply partial, not total, differentiation.)

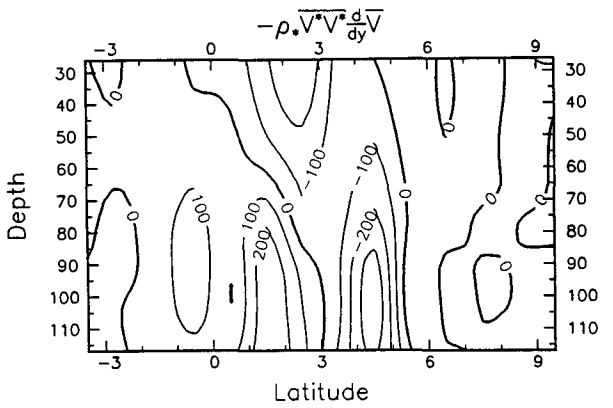

FIG. 14. As in Fig. 13, but for $-\rho_* \overline{V^* V^*}(\partial \bar{V}/\partial y)$. These values are relatively small: the positive maximum is significant at 1.2 rms errors, and the negative maxima are significant at about 2 rms errors.

through this term is 25×10^{-6} erg cm^{-3} s^{-1} (2.5 μW m^{-3}), much less than the 234×10^{-6} erg cm^{-3} s^{-1} from the term above. This result is in contradiction to Hansen and Paul's (1984) finding that this term contributes about 40% as much as the term above to the eddy energy production. The eddy energy loss averaged from 3° to 6°N is -73×10^{-6} erg cm^{-3} s^{-1}.

Two components of low-frequency to eddy kinetic energy production can also be estimated. The term $-\rho_* \overline{\tilde{U}^* \tilde{V}^*}(\partial \bar{U}/\partial y)$ (Fig. 15) produces an eddy energy loss from 1° to 3°N. This loss is significant at about 1.4 rms errors, as is the smaller loss region from 5°N to 6°N. The second low-frequency to eddy kinetic energy production term, $-\rho_* \overline{V^* \tilde{V}^*}(\partial \bar{V}/\partial y)$, is quite small in general, only occasionally exceeding 100 $\times 10^{-6}$ erg cm^{-3} s^{-1}. However, the eddy energy gain from this term between 1°S and 0.5°N is significant at 2 rms errors, and partially offsets the loss to the north due to the term in Fig. 15. The two terms sum to an average of -32×10^{-6} erg cm^{-3} s^{-1} (−3.2 μW m^{-3}) in the band between 1°S and 3°N, and to -42×10^{-6} erg cm^{-3} s^{-1} between 3° and 6°N. The implication is that the high-frequencies lose kinetic energy to the low frequencies on average. This conclusion will be discussed further in section 7c of the summary.

The total eddy kinetic energy production due to the four terms discussed above is shown in Fig. 16. The eddy energy production is dominated by $-\rho_* \overline{U^* V^*}(\partial \bar{U}/\partial y)$, but the strong peak of this term at 0°–2°N has been reduced and broadened southward by the two low-frequency to eddy energy production terms. The eddy energy losses to the north at 2°–5°N are contributed mostly by the mean to eddy conversion term $-\rho_* \overline{V^* V^*}(\partial \bar{V}/\partial y)$. The errors of the combined term are somewhat larger than for $-\rho_* \overline{U^* V^*}(\partial \bar{U}/\partial y)$ alone, and the maxima in the combined term are at best only significant at about 1.5 rms errors due to the partial cancellation of terms.

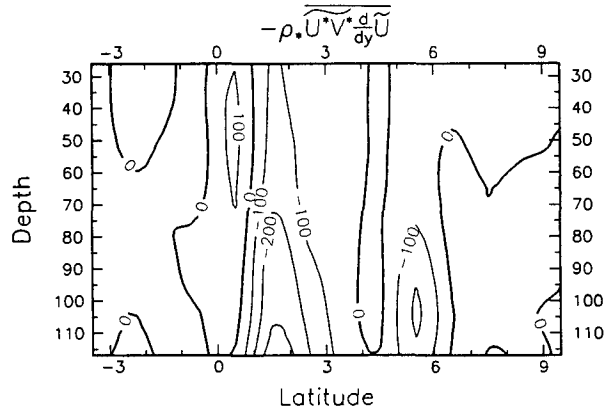

FIG. 15. The low-frequency–to–eddy kinetic energy conversion term $-\rho_* \overline{\tilde{U}^* \tilde{V}^*}(\partial \bar{U}/\partial y)$, in 10^{-6} erg cm^{-3} s^{-1}. Note the negative values in the region of strong mean flow to eddy energy conversion at 0° to 3°N: while the eddies gain energy from the mean flow they lose some energy to the low-frequency flow (significant at about 1.4 rms errors).

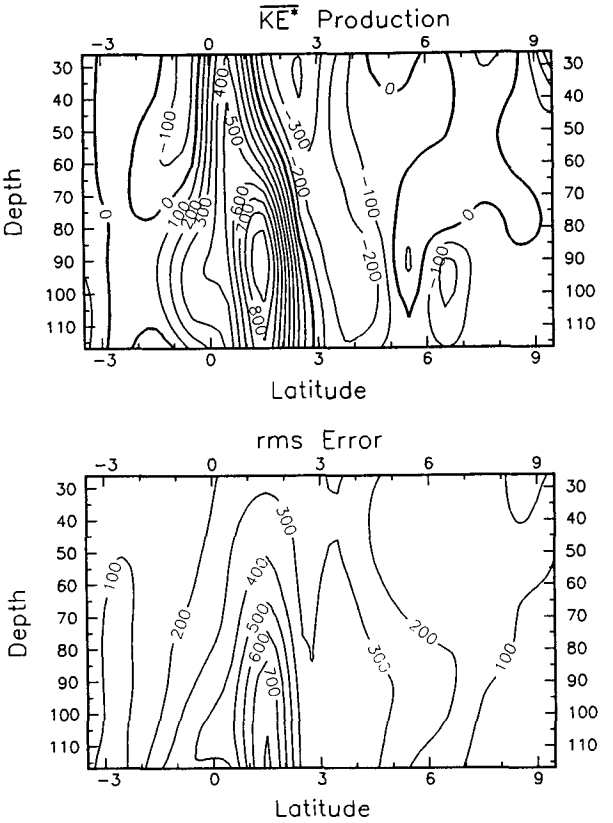

FIG. 16. The sum of eddy kinetic energy production calculated, i.e. the sum of the last four terms on the rhs of Eq. (3.3), with rms errors.

b. Potential energy production

Only one component of the baroclinic conversion of mean potential energy to eddy potential energy can be estimated with the present data [see (3.5)], namely $-C\overline{\rho^* V^*}(\partial\bar{\rho}/\partial y)$ shown in Fig. 17. The potential energy production is small south of 4°N, and slightly negative from 0° to 2°N (corresponding to the upgradient density flux previously noted in Fig. 12b). It will be shown in section 6 that the values in this region are small year-round, indicating that little baroclinic energy conversion is associated with the barotropic energy conversion found near the equator above. This result differs from the findings of Hansen and Paul (1984) further to the east, where the baroclinic energy conversion was as strong as the barotropic at 0°–2°N, and is probably an indication of a true zonal difference in the character of the instability, since the equatorial front is stronger and closer to the equator at 100°–130°W, where Hansen and Paul's measurements were taken, than at 150°–158°W. Notice in Fig. 17 that there is baroclinic eddy energy production (significant at a little more than one rms error) associated with the equatorial front near the surface at 3°–6°N. However, it will be shown in section 6 that this energy production is temporally (and, therefore, physically) unrelated to the barotropic kinetic energy production near the equator. The energy production at the equatorial front does not correspond to distinct maxima of eddy variance (Figs. 5 and 9) or covariance (Fig. 12b), but the covariance in Fig. 12b at the front is significant at about two rms errors. This density flux produces a maximum of potential energy production due to multiplication by the large ratio of horizontal to vertical mean density gradients that is typical of fronts. The average of the eddy energy production between 3° and 6°N, over the whole depth range observed, is 119×10^{-6} erg cm^{-3} s^{-1} (11.9 μW m^{-3}).

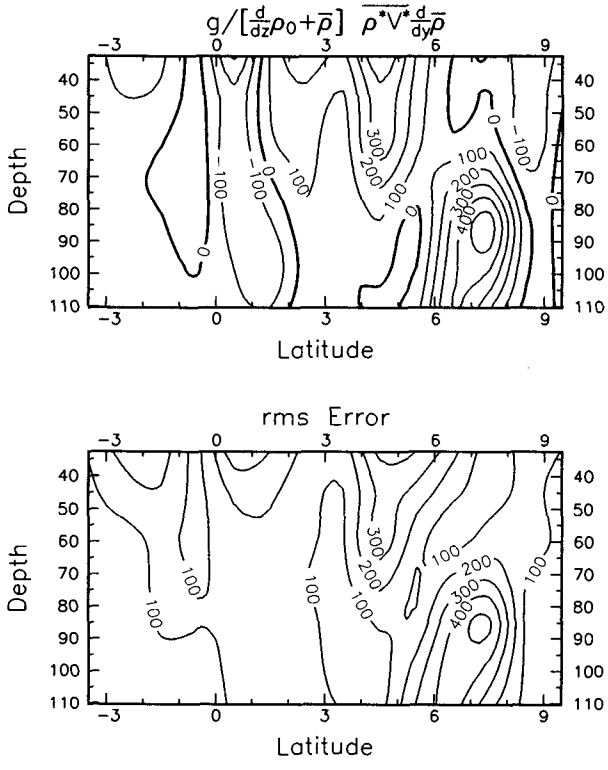

FIG. 17. The mean eddy potential energy conversion term $-C\overline{\rho^* V^*}(\partial\bar{\rho}/\partial y)$, with rms errors. Units are 10^{-6} ergs cm^{-3} s^{-1}. Note the large eddy energy gain in the NECC thermocline and at the equatorial front, 3°–6°N. These peaks are significant at a little over one rms error.

The numerically modeled $\overline{V^* T^*}$ covariances shown in Philander et al. (1986) suggest a subsurface maximum which is below 117 m depth at 154°W. Therefore, it is possible that a region of larger near-equatorial baroclinic eddy energy production has been missed due to the shallowness of the present data. In the Atlantic Ocean, Weisberg and Weingartner (1988) have not found significant baroclinic eddy energy production near the equator.

A novelty in Fig. 17 is the large baroclinic eddy energy production found in the thermocline of the NECC. The feature is only slightly greater than one rms error from zero, but the suggestion of baroclinic instability of the NECC is intriguing, and has not been previously made by any analytic or numerical model. This baroclinic energy production coincides in latitude and depth with the previously noted maximum in U^{*2} and a weaker maximum in V^{*2} (Figs. 5 and 9). In section 6 it will be shown that this eddy energy production coincides with NECC velocity variance maxima in time as well, and that this time variability is distinguishable from the variability of both the near-equatorial barotropic instability and the equatorial front instability. The average eddy energy production between 6° and 10°N is 91×10^{-6} erg cm^{-3} s^{-1} (9.1 μW m^{-3}). The fact that the strongest eddy covariance and variance values appear to be confined below 50 m depth suggests why these eddies have not been noticed in previous drift-buoy and ship-drift data. The confinement of the eddy variance to a narrow region of the NECC thermocline is consistent with theoretical models of baroclinic instability. Talley (1983) has shown that fluctuations due to the strongest instabilities of eastward jets are laterally trapped in the jet, which also implies vertical trapping. [N.B., use of $\partial\rho_0/\partial z$, instead of $\partial(\rho_0 + \bar{\rho})/\partial z$, in $C(z)$ for the potential energy production results in nearly a tripling of the implied eddy production in the NECC thermocline, with concomitantly reduced magnitudes to the south.]

The conversion of low-frequency potential energy to eddy potential energy (sixth term on the rhs of 3.4) is much smaller than the conversion from mean potential energy. The low-frequency conversion appears

to reinforce the production of eddy energy near-surface at 3° to 6°N, and to result in an eddy energy loss near-surface at 8° to 9°N. Neither of these features (at 150–200 $\times 10^{-6}$ erg cm^{-3} s^{-1}) are much more than one rms error from zero.

c. *Advection and diffusion*

There are three terms in the simplified eddy kinetic energy equation (3.3) involving the advection of eddy kinetic energy. The advection of eddy kinetic energy by the mean meridional currents, $-\bar{V}(\partial\overline{\mathrm{KE}^*}/\partial y)$, is quite weak, rarely exceeding 100×10^{-6} erg cm^{-3} s^{-1} in magnitude. The average of this term between 1°S and 3°N is 10×10^{-6} erg cm^{-3} s^{-1} (1 μW m^{-3}), while between 3° and 6°N it is 17×10^{-6} erg cm^{-3} s^{-1}. The alternative form of the term, obtained by employing the continuity equation in (3.2), i.e., $-[\partial(\bar{V}\overline{\mathrm{KE}^*})/\partial y]$, has a similar pattern but substantially larger values. The advection of eddy kinetic energy by the low-frequency meridional velocity, $\tilde{V}(\partial\overline{\mathrm{KE}^*}/\partial y)$, is also weak, being only occasionally greater than 100×10^{-6} erg cm^{-3} s^{-1} in magnitude. The last advection term, the eddy self advection $-\overline{V^*(\partial \mathrm{KE}^*/\partial y)}$, is larger and possibly important in the redistribution of eddy kinetic energy in space, especially in the band from 1°S to 6°N. This term is shown in Fig. 18. The positive maximum at about 2.5°N and the negative band at about 4°N are better than 1 rms error from zero. The alternative form including continuity, $-[\partial(\overline{V^*\mathrm{KE}^*})/\partial y]$, is very similar to Fig. 18 with only slightly larger magnitudes. The net contribution of the term to the eddy energetics, 90×10^{-6} erg cm^{-3} s^{-1} (9 μW m^{-3}) in the 1°S to 3°N band, and -22×10^{-6} erg cm^{-3} s^{-1} in the 3° to 6°N band, is fairly small.

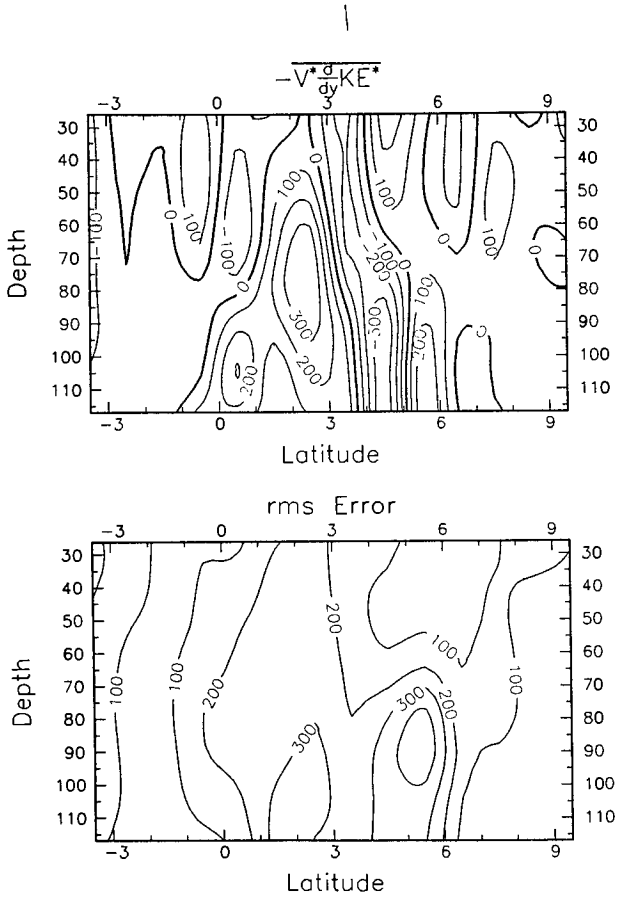

FIG. 18. The eddy self-advection of eddy kinetic energy, $-\overline{V^*(\partial \mathrm{KE}^*/\partial y)}$, in 10^{-6} erg cm^{-3} s^{-1}. The values are larger than the mean flow advection, but the two largest maxima are significant at only about 1.5 rms errors.

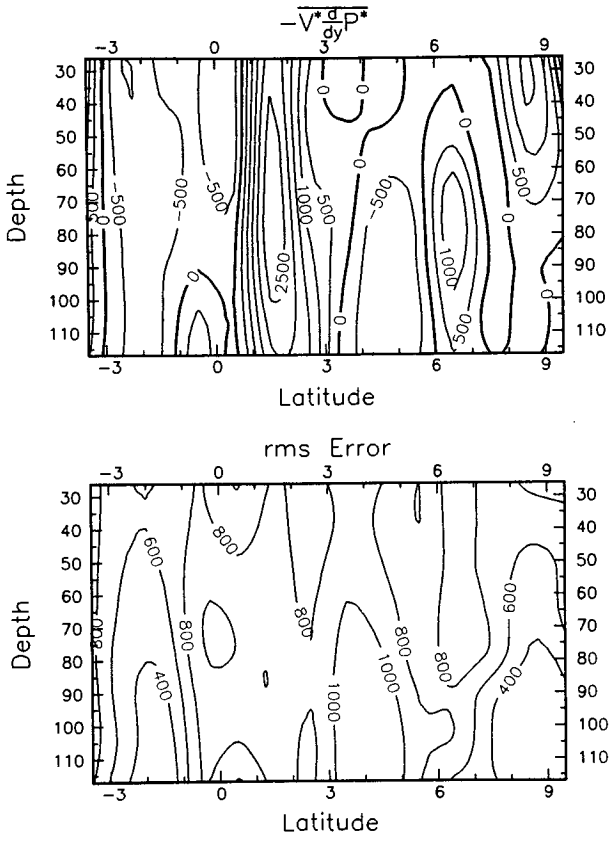

FIG. 19. The meridional diffusion of eddy kinetic energy, $-\overline{V^*(\partial P^*/\partial y)}$, with rms errors. Units are 10^{-6} erg cm^{-3} s^{-1}. This term represents a redistribution of eddy energy in space. Note the very large eddy energy gain at 1° to 3°N, where the large mean flow to eddy kinetic energy conversion is found (Fig. 13). This peak is significant at over 3 rms errors. It is possible that the meridional diffusion is cancelled to some extent by the unestimated zonal diffusion, $-\overline{U^*(\partial P^*/\partial x)}$, or vertical diffusion, $-\overline{W^*(\partial P^*/\partial z)}$.

The meridional divergence of eddy pressure work, $-\overline{V^*(\partial P^*/\partial y)}$, shown in Fig. 19, indicates a substantial diffusive redistribution of energy in space. The major feature is a region of large eddy energy gain between 1° and 3°N which coincides with the eddy variance and eddy energy production peaks of the barotropic

instability. This feature is significant at over 3 rms errors. The shallow eddy energy gain at 8°–9°N is also significant at more than 2 rms errors. The alternative form of this term, $-[\partial(\overline{V^*P^*})/\partial y]$, retains the two significant features almost unchanged but has greatly increased background levels. The average contribution of the pressure work divergence term in Fig. 19 to the 1°S to 3°N band is 771×10^{-6} erg cm^{-3} s^{-1} (77.1 μW m^{-3}), larger even than the mean flow to eddy kinetic energy production terms. It is possible, though, that the missing component of pressure work divergence, $-\overline{U^*(\partial P^*)/\partial x)}$, substantially cancels this one, which will occur when eddy velocities are along eddy pressure contours. In the Atlantic, Weisberg and Weingartner (1988) found instantaneous values of $-\overline{V^*(\partial P^*/\partial y)}$ with magnitudes as large as our average values at 1°–2°N, but with opposite sign. They also found at least partial cancellation between the two horizontal components of pressure work divergence, and note as well that $-\overline{W^*(\partial P^*/\partial z)}$ was small. The latter term must be important somewhere near the equator in the eastern Pacific, because the instability fluctuations are known to excite vertically propagating waves (e.g., Weisberg 1987). Downward radiation of eddy energy is also an important energy sink in numerical models that simulate the instabilities of equatorial Pacific currents (e.g., Cox 1980).

The mean eddy potential energy is shown in Fig. 20a. There are maxima from 4° to 6°N near the surface and at 6°N in the thermocline which are probably associated with the eddy potential energy production maxima near these locations (see Fig. 17). The increased energy in the equatorial thermocline could be due to equatorially trapped internal waves, or to a deeper baroclinic instability as mentioned in section 5b. The large near-surface potential energy values at 2°S are not associated with any appreciable eddy potential energy production. As was noted in section 3a, our substitution of $\rho^*[\partial(\rho_0 + \bar{\rho})/\partial z]^{-1}$ for the vertical displacement of water parcels in our definition of $\overline{PE^*}$ can lead to inaccuracies in the mixed layer. In particular, at 2°S near the surface the stratification is so low that the rms density variations lead to estimated rms displacements of over 100 m. In reality, the parcels need come from no further than the base of the mixed layer. A calculation of $\overline{PE^*}$ using a more accurate estimate of displacement variance is shown in Fig. 20b. Here ζ^{*2} is estimated as the square of the distance through which a fluid parcel must be raised in order to produce a density signal equal to the observed root density variance at each location. Figure 20b shows no maximum at all at 2°S, but confirms the presence of the near-surface maximum at 4°–6°N. Values of potential energy below the mixed layer are almost unchanged. Therefore we will dismiss as spurious the near-surface maximum of $\overline{PE^*}$ at 2°S.

The mean meridional advection of eddy potential energy, $-\frac{1}{2}C\bar{V}(\partial\overline{\rho^{*2}}/\partial y)$ (not shown), appears to be as unimportant as the corresponding advection of $\overline{KE^*}$. The low-frequency advection, $-\frac{1}{2}C\tilde{V}(\partial\widetilde{\rho^{*2}}/\partial y)$, is only slightly larger than the mean advection. It contributes a small eddy energy gain (peak value of 200×10^{-6} erg cm^{-3} s^{-1}) in the NECC slightly south of the baroclinic eddy energy production in the NECC thermocline. The self-advection term, $-\frac{1}{2}C\overline{V^*(\partial\rho^{*2}/\partial y)}$, is also small; some loss of eddy energy occurs in the NECC thermocline and near-surface at 8°–9°N. Overall then the advection terms in the eddy potential energy equation are not of great importance.

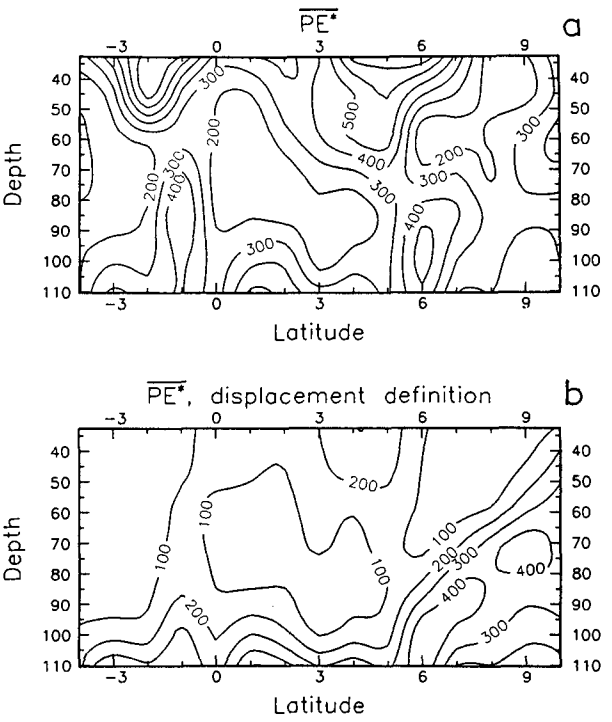

FIG. 20. The eddy potential energy in erg cm^{-3}. $\overline{PE^*}$ as defined in section 3a is shown in Fig. 20a. Figure 20b shows a more accurate estimate of $\overline{PE^*}$ using vertical displacement variance rather than density variance as in (a). The standard definition in (a) over-estimates $\overline{PE^*}$ in the mixed layer, and produces a spurious near-surface maximum at 2°S.

6. Temporal variability

The near-surface mesoscale fluctuations have amplitudes that are known to be strongly seasonally dependent (e.g., Philander et al. 1985). Previous observational (Hansen and Paul 1984) and theoretical (Philander et al. 1986) studies of these waves have concentrated on the most energetic time periods of the near-equatorial fluctuations (i.e., northern or boreal summer–fall) in order to more clearly isolate the fluctuation characteristics. Consequently, we present in this

section a variety of computations made from averages over time periods shorter than our total one year data length. The notation $(\hat{\ })$ will refer to an average over one of the short time periods defined below. The eddy energy conservation equations for fixed time periods much shorter than one year, but much longer than the fluctuation time scale, are as follows, under the assumptions leading to (3.3) and (3.5):

$$\frac{\partial}{\partial t}\widehat{\mathrm{KE}^*} = -\hat{V}\frac{\partial}{\partial y}\widehat{\mathrm{KE}^*} - \widehat{V^*\frac{\partial}{\partial y}\mathrm{KE}^*} - \widehat{V^*\frac{\partial}{\partial y}P^*} - U^*\widehat{V}^*\frac{\partial}{\partial y}\hat{U} - V^*\widehat{V}^*\frac{\partial}{\partial y}\hat{V}, \quad (6.1)$$

$$\frac{\partial}{\partial t}\widehat{\mathrm{PE}^*} = -\frac{C}{2}\hat{V}\frac{\partial}{\partial y}\widehat{\rho^{*2}} - \frac{C}{2}\widehat{V^*\frac{\partial}{\partial y}\rho^{*2}} - C\rho^*\widehat{V}^*\frac{\partial}{\partial y}\hat{V}, \quad (6.2)$$

where KE*, PE*, and C are defined as in (3.2) and (3.4) but with $W^* \equiv 0$, and the residuals, denoted by asterisks, are those defined before in (3.1). Only those terms in (6.1) and (6.2) which relate to the strongest eddy energy production will be shown here. In addition, the temporal variability of the important variances and covariances will be discussed.

In an effort to emphasize the seasonal variability of the zonal equatorial mean currents and the mesoscale activity, the data were divided into three non-overlapping time periods. These are noted on Fig. 4, which shows the variations of vertically averaged zonal velocity as a function of time, and on Fig. 1, which shows low-pass filtered MCM velocities at the equator. From these figures the following periods were chosen, for the indicated reasons. The mean zonal velocity for each time period is shown in Fig. 21, and the mean density is in Fig. 22. Note that the dates below refer to the time of equator crossing of the first and last sections included in each time period.

Period A: 7/27/79–11/19/79
The EUC, SECN, and NECC are all well-developed, and the dominant period of the oscillations in meridional velocity (Fig. 1) is longer than in subsequent months.

Period B: 12/16/79–3/10/80
The SECN and NECC are well-developed, but the EUC is weak. From the mooring data (Fig. 1) it is seen that at the end of this time period the eastward currents at the equator begin to increase rapidly.

Period C: 4/5/80–6/8/80
The EUC and NECC are well-developed, but the SECN is very weak. The NECC is not as strong here as in the other time periods.

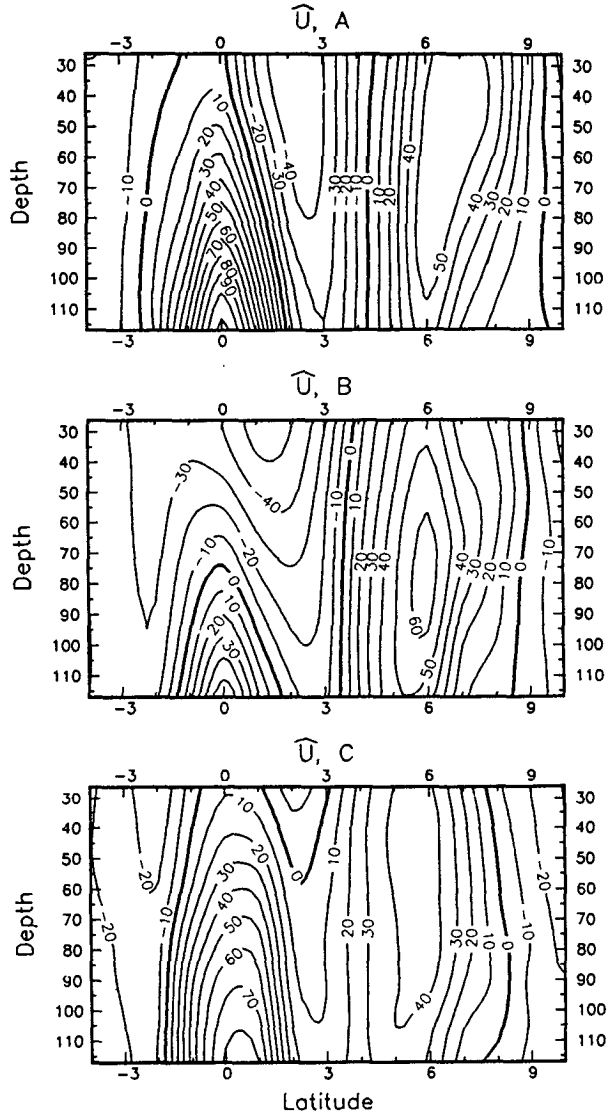

FIG. 21. The mean zonal velocity, $\hat{U}$, during time periods, A, B and C. Units are cm s^{-1}. See Figs. 1 and 4 and the text for a description of the time periods. Note the changing strengths of the currents, especially the EUC and the part of the SEC north of the equator (SECN), and the changing intensity of the shear between them.

Two sections of data in late March are not included in B or C above since they occur in a transitional time of rapidly accelerating equatorial eastward currents (Fig. 1) and would only serve to weaken the contrasts between the average currents in B and C if included in either. No such data deletion occurred between time periods A and B due to the already large gap between the sections. Serendipitously, time period A corresponds well with the data coverage (6/9/79–10/27/

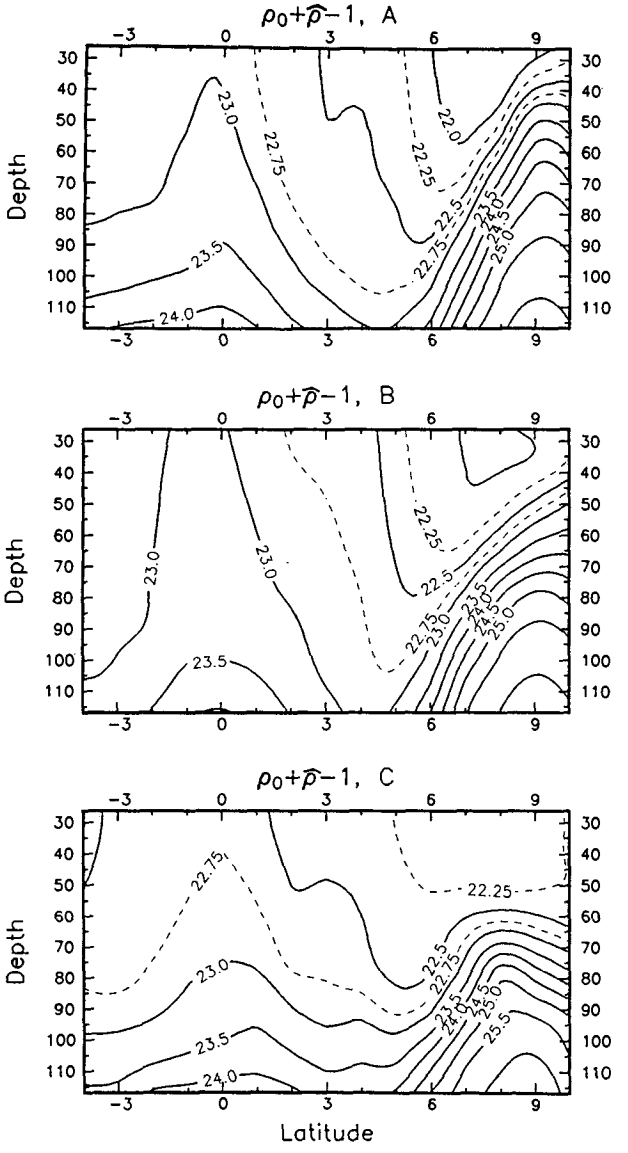

FIG. 22. As in Fig. 21 but for the mean density, in 10^3 g cm^{-3}.

79) employed by Hansen and Paul (1984) and with the averaging period (7/15–12/15) used by Philander et al. (1986). [N.B., although it is stated in Fig. 5 of Philander et al. (1986) that the averages are for one year, in fact the averaging interval is only 7/15–12/15 (W. Hurlin, private communication 1988).] The differences between the mean zonal velocities in Fig. 21 range up to 60 cm s^{-1}. Differences greater than 10 cm s^{-1} are generally significant with a 2 to 5 cm s^{-1} rms error. The differences between the mean densities (Fig. 22) range from 0.03 g cm^{-3} near the surface to 0.3 g cm^{-3} in the pycnocline; the former are significant at better than 1 rms error and the latter at about 3 rms errors.

a. Momentum and heat fluxes

The meridional flux of zonal momentum, $\widehat{U^*V^*}$, is strikingly different in the three time periods, as shown by Fig. 23. In time period A, a broad positive peak in $\widehat{U^*V^*}$ occurs from 2°S to 3°N, with little in the way of negative values or significant amplitudes away from this region. This peak is significant at about the 2 rms error level (3 rms errors near the surface). The magnitude and meridional structure of the peak are quite comparable to fluxes generated by Philander et al.'s (1986, Fig. 6) numerical model at 154°W when $A_h = 1$

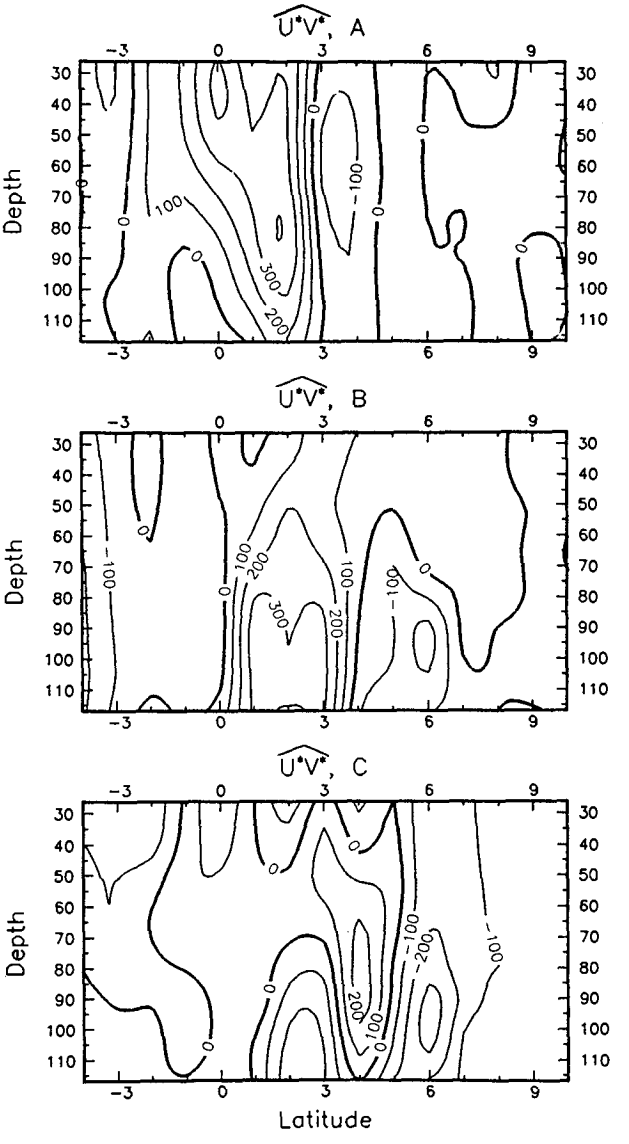

FIG. 23. As in Fig. 21 but for the mean residual covariance, $\widehat{U^*V^*}$, in cm^2 s^{-2}. Note that the positive values near 2°N appear to be associated with strong shear between the EUC and the SECN, which occurs in time periods A and B.

$\times 10^7$ cm^2 s^{-1}. The major difference is the apparent deeper penetration of significant momentum fluxes in the data versus the model results. Hansen and Paul's (1984) observations further east (at a 30 m drogue depth) reach 1500 cm^2 s^{-2} just south of the equator, compared to 400 cm^2 s^{-2} here, although their large values are not significantly different from zero at the equator at 2 rms errors. Between 1° and 2°N they find values of 400–500 cm^2 s^{-2} which are significant at 2 rms errors. Excluding Hansen and Paul's questionable values at and just south of the equator, their covariances are quite comparable to those at 30 m in Fig. 23a, even in the suggestion of a region of negative values at 4°N (significant here at 1.6 rms errors).

For time period B in the winter season, a broad positive $U^*\hat{V}^*$ peak is still evident, but now is deeper and further north than in A, the summer/fall season. This peak is significant at 2 rms errors, as are the negative values which have appeared in the NECC. It is perhaps significant that, relative to period A, the deeper momentum fluxes in period B are co-incident with a deeper region of maximum EUC–SECN lateral shear (Fig. 21).

In time period C, $U^*\hat{V}^*$ shows a pattern of alternating positive and negative maxima from 2° to 7°N, a band in which the meridional shear of the mean zonal currents is fairly weak (Fig. 21c). Although these maxima are significant at about 1.5 rms errors (well over 2 rms errors for the negative peak in the NECC), their association with weak mean shears implies a lesser importance in the eddy energetics, as is shown below.

Figure 24 shows the meridional heat flux, $\hat{V}^*\hat{T}^*$, for the three time periods. In period A, the peaks at 3°S, 1°N, and 9°N are all significant at the 2 rms error level, but the values appear to be quite small relative to those found by Hansen and Paul (1984) to the east. Hansen and Paul's estimates for a nominal 30 m depth were as large as −25°C cm s^{-1} at 1°–2°N and 10°C cm s^{-1} south of the equator. We do not see in Fig. 24 the picture of eddy heat flux convergence on the equator found by Hansen and Paul in the east and by Luther et al. (1987) at 140°W from 10 to 120 m. Using the entire 1979–80 NORPAX current meter array at 152°–153°W, Bryden and Brady (1989) found a small, highly depth dependent heat flux convergence at the equator. Given the spatial and temporal differences between the ADCP and the current meter measurements, it is hard to draw any conclusions about the disparities. The Philander et al. (1986) calculation of $\hat{V}^*\hat{T}^*$ (their Fig. 6) shows only a single negative peak of −4°C cm s^{-1} at 3°N in the domain 0–110 m, 4°S–10°N, which is not consistent with Fig. 24a.

In period B, the negative flux at 3°S has vanished as has the near-surface peak at 9°N. The positive flux on the equator has weakened, negative fluxes have appeared to the north, and positive fluxes are beginning to appear in the NECC thermocline. All three of these features contain values that are significant at 2 rms errors.

The C (spring) time period has large positive meridional heat fluxes in and slightly above the thermocline from the equator to 9°N which are significant at 1.5 to 2 rms errors. The largest values, in the NECC thermocline, are responsible for the eddy potential energy production noted at this latitude in section 5, as will be shown below.

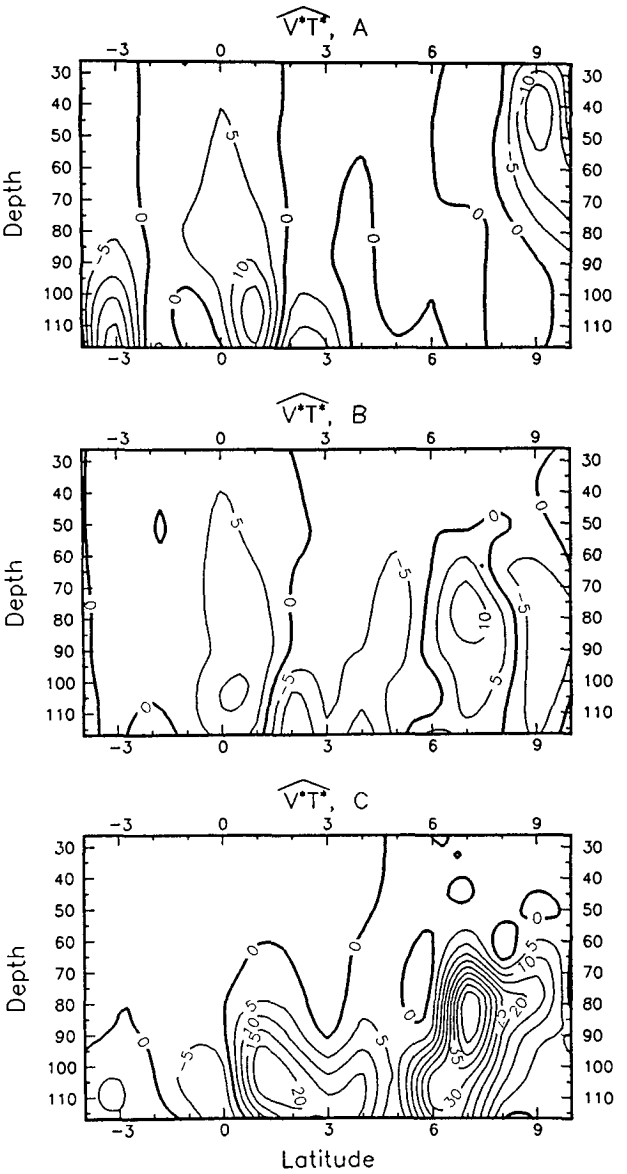

FIG. 24. As in Fig. 21, but for heat flux, $\hat{V}^*\hat{T}^*$, in °C cm s^{-1}. The strong, positive (downgradient) flux in the thermocline at 6° to 8°N occurs mostly in time period C.

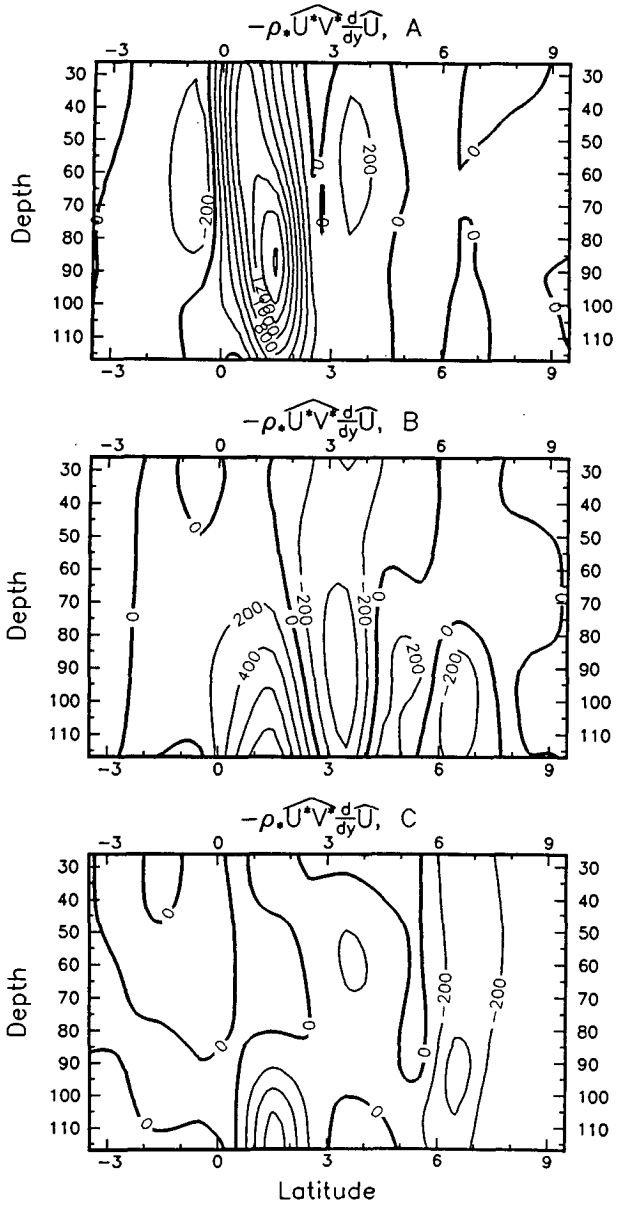

FIG. 25. As in Fig. 21, but for the mean flow to eddy kinetic energy conversion term, $-\rho_* \widehat{U^*V^*}(\partial \hat{U}/\partial y)$, in 10^{-6} ergs cm^{-3} s^{-1}. The strong gain in eddy energy at 0° to 2°N found in the yearly average (Fig. 13) is confined here to period A. In B, although the Reynolds stress is still large in this region (Fig. 23), the net eddy energy gain is small. Note, however, that the ADCP data do not clearly determine the vertical extent of the energy gain region. In C an eddy energy loss occurs in this region as well as in the NECC.

b. *Eddy energy production and diffusion*

The eddy kinetic energy production term, $-\rho_* \widehat{U^*V^*}(\partial \hat{U}/\partial y)$, is shown in Fig. 25 for each time period. Time period A has a remarkably simple picture of eddy energy production from 0°–2°N, peaked at 90 m in the high mean shear region between the EUC and SECN (see Fig. 21a), with small values elsewhere. The peak is significant at 1.4 rms errors at its maximum, and at up to 2 rms errors near the surface. A small positive peak at 3°–4°N (significant at 1.1 rms errors) indicates a possible weak involvement of the SECN–NECC shear in the eddy generation process. The average rate of eddy energy production from 1°S to 3°N is 422×10^{-6} erg cm^{-3} s^{-1} (42 μW m^{-3}), a rate sufficient to replace the eddy kinetic energy in the same region (469 erg cm^{-3}) in about 13 days. In the same time period but further to the east, Hansen and Paul (1984) found near-surface (30 m) values for this term approaching 500 μW m^{-3}, compared to our largest values at 30 m of 110 μW m^{-3}. Again, Hansen and Paul's largest values are not very reliable; their more reliable estimates of $\widehat{U^*V^*}$ at 0.75°–1.75°N yield energy production values closer to 200 μW m^{-3}. Their average rate of eddy energy production between 7°S and 7°N is 44 ± 23 μW m^{-3}, and they also show a weak involvement of the SECN–NECC shear.

In time period B there is still eddy energy production from 0° to 2°N (significant at 1.7 rms errors), but it is weaker and deeper than in A, coinciding with the weaker and deeper EUC-SECN lateral shear. There is also a fairly strong eddy energy loss region at 2°–4°N (significant at about 1 rms error). The total average rate of eddy energy production in this period between 1°S and 3°N is 112×10^{-6} erg cm^{-3} s^{-1} (11.2 μW m^{-3}), while between 3° and 6°N it is -120×10^{-6} erg cm^{-3} s^{-1}, so that the net eddy energy production is insignificant. Of course, given the peak structure at 0°–2°N in Fig. 25b, the ADCP data studied here may have missed a region of strong eddy energy production below 117 m in this time period.

There are no significant regions of eddy energy gain in time period C, only losses, with the largest losses at 1°–2°N below 90 m (significant at 1 rms error) and between 6° and 8°N (significant at 1.5 rms errors). The average rate of eddy energy production from 1°S to 3°N is -81×10^{-6} erg cm^{-3} s^{-1} (−8.1 μW m^{-3}), from 3°N to 6°N it is -38×10^{-6} erg cm^{-3} s^{-1}, and between 6°N and 10°N it is -158×10^{-6} erg cm^{-3} s^{-1}.

The A and B plots in Figs. 25 and 21 suggest that the EUC is an important contributing factor in the instability mechanics. Given the fact that the EUC is strong in period C as well, we must conclude that a westward SEC and an eastward EUC are both necessary for significant eddy kinetic energy production to occur at these longitudes.

The eddy kinetic energy production term, $-\rho_* \widehat{V^*V^*}(\partial \hat{V}/\partial y)$, has a latitude–depth structure in each time period (not shown) that is similar to the mean field in Fig. 14. However, time period B has the largest values, reaching 500×10^{-6} erg cm^{-3} s^{-1} near

the equator with better than 1 rms error significance. Time period A has magnitudes similar to Fig. 14, while C is much weaker.

The spatial patterns (not shown) of the meridional divergence of eddy pressure work, $-\widehat{V^*(\partial P^*/\partial y)}$, differ substantially between time periods. In A, the latitude band of eddy energy gain (significant at 2 rms errors) is narrowly confined between 1° and 2.5°N, as in Fig. 19, with negative values at most other latitudes. In B, the eddy energy gain occurs from 0° to 4°N and 6°–8°N, with maxima significant at better than 2 rms errors. In C, significant gain and loss is concentrated in alternating narrow latitude bands north of 4°N.

The eddy potential energy production term, $-C\widehat{\rho^* V^*}(\partial\hat{\rho}/\partial y)$, is presented for each time period in Fig. 26. In period A, and to a lesser extent in B, there is a small eddy potential energy loss near the equator from 0° to 2°N (significant at 1.4 rms errors in both A and B). In A the maximum value at 30 m in this region exceeds -600×10^{-6} erg cm^{-3} s^{-1} (-60 μW m^{-3}), compared with Hansen and Paul's positive 200–300 μW m^{-3} between 0° and 2°N. The average rate of eddy energy production from 1°S to 3°N in A is -54×10^{-6} ergs cm^{-3} s^{-1} (-5.4 μW m^{-3}), compared to Hansen and Paul's value of 52 ± 21 μW m^{-3} for 7°S to 7°N. A small amount of eddy energy production appears near the surface from 4° to 6°N (significant at 0.9 rms errors) with a peak value of 640×10^{-6} erg cm^{-3} s^{-1} (64 μW m^{-3}). This energy production is coincident with a near-surface maximum in $\overline{PE}^*$ (Fig. 20). The average eddy potential energy production between 3° and 6°N is 94×10^{-6} erg cm^{-3} s^{-1} (9.4 μW m^{-3}). There appears to be an additional loss of eddy potential energy in A near-surface at 8°–10°N, which is significant at 1.5 rms errors.

In period B, the near-surface eddy potential energy production on the equatorial front at 3°–6°N has intensified to a peak of 880×10^{-6} erg cm^{-3} s^{-1} (88 μW m^{-3}), but it is still significant at only 1 rms error. Concurrently, the equatorial front appears to be better developed in period B than in period A; note the deeper penetration of the steeply sloping isopycnals at 4°–5°N in period B (Fig. 22). We also see the beginning of eddy energy production in the NECC thermocline. The energy loss near-surface in A at 8°–10°N has nearly vanished, as has the loss near the equator. The average eddy energy gain from 3° to 6°N is 272×10^{-6} erg cm^{-3} s^{-1} (27.2 μW m^{-3}), while between 6 and 10°N it is 63×10^{-6} erg cm^{-3} s^{-1}. The eddy potential energy production between 3° and 6°N is sufficient to replace the average eddy potential energy in the same region (369 erg cm^{-3}) in about 16 days.

In C, the near-surface eddy potential energy production at 3°–6°N has almost vanished, possibly due to the weakening of the equatorial front (Fig. 22c), while the production in the NECC thermocline is very

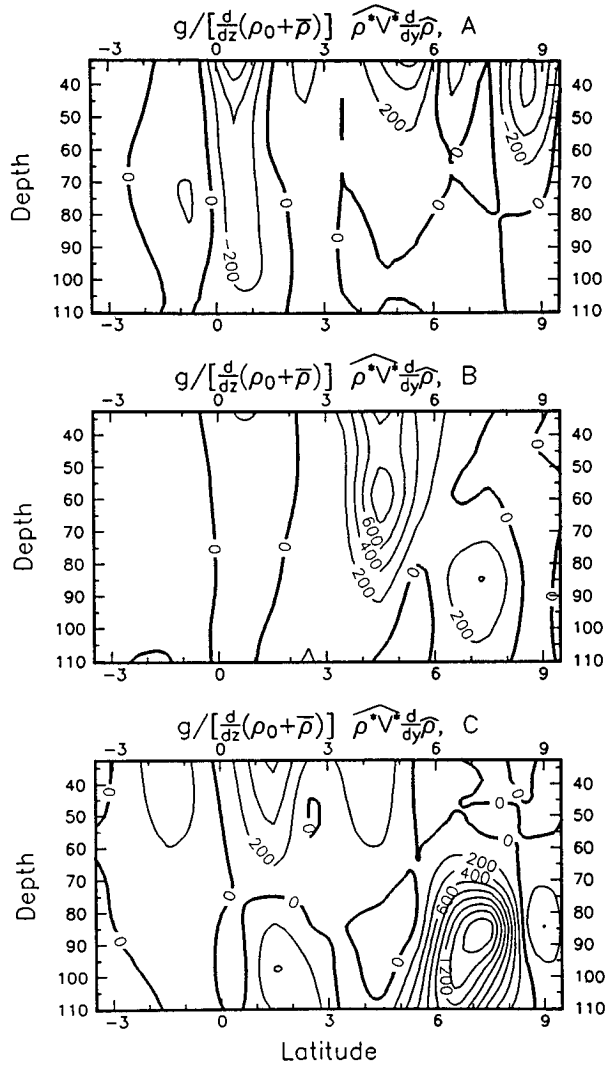

FIG. 26. As in Fig. 25 but for the mean flow to eddy potential energy conversion term, $-C\widehat{\rho^* V^*}(\partial\hat{\rho}/\partial y$. Note the large eddy energy gain at the equatorial front, 3°–6°N, in period B, and in the thermocline between 5° and 8°N during period C. Note also the small loss of eddy energy between 0° and 2°N in period A, during the large gain in kinetic energy there.

large, reaching a value of 1680×10^{-6} erg cm^{-3} s^{-1} (168 μW m^{-3}), which is significant at only 1.1 rms errors. The average rate of production in the 1°S–3°N band and the 3°–6°N band is only 17×10^{-6} erg cm^{-3} s^{-1} and 125×10^{-6} erg cm^{-3} s^{-1}, respectively, while in the 6°–10°N band it is 277×10^{-6} erg cm^{-3} s^{-1}. The latter eddy potential energy production is sufficient to replace the eddy potential energy in the 6°–10°N region (198 ergs cm^{-3}) in about 8 days. The existence of this potential energy production and the energy production at the equatorial front, in time periods completely different from that of the kinetic energy pro-

duction near the equator, establishes that all three phenomena are independent. The implication is that the equatorial front and the NECC are baroclinically unstable at these longitudes during parts of the year.

c. *Variances*

Figures 27 and 28 show the variances $\widehat{U^{*2}}$ and $\widehat{V^{*2}}$ for the three time periods. In time period A, we found previously (Fig. 25) a strong eddy kinetic energy production region confined between 0° and 2°N and

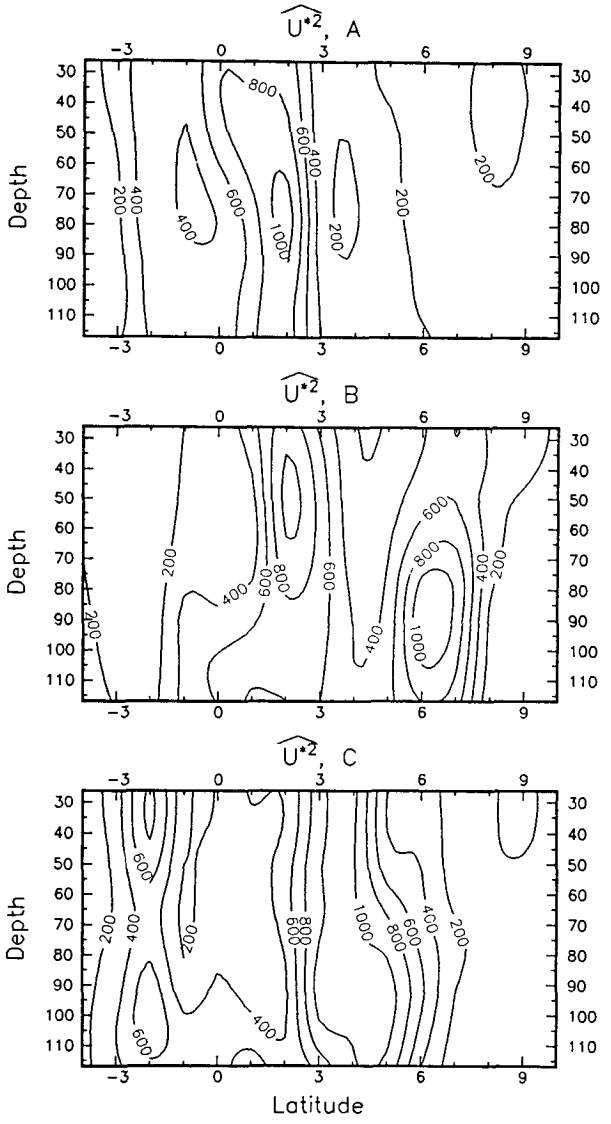

FIG. 27. As in Fig. 21 but for the eddy zonal velocity variance, $\widehat{U^{*2}}$, in cm^2 s^{-2}. The barotropic eddy energy production in period A from 0° to 2°N (Fig. 25) appears to correspond to increased local variance.

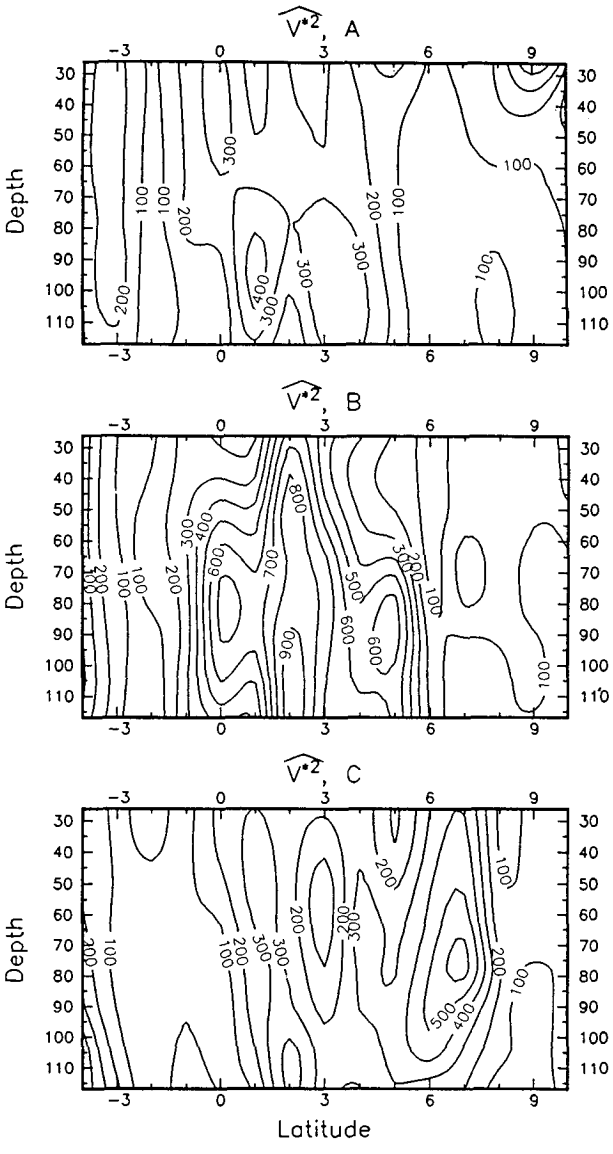

FIG. 28. As in Fig. 27 but for meridional variance, $\widehat{V^{*2}}$. The small variance maximum in period C, 6° to 7.5°N, may be due to the baroclinic eddy energy production there (Fig. 26).

peaked at 1°N and 90 m depth. Apparently associated with this energy production is a $\widehat{U^{*2}}$ maximum similarly confined and peaked at 2°N and 80 m. A $\widehat{V^{*2}}$ maximum is also present but is more broadly distributed between 1°S and 4°N and has maxima less than half the magnitude of the $\widehat{U^{*2}}$ maximum. The averages of these variances in the 1°S–3°N band are 653 cm^2 s^{-2} for U and 264 cm^2 s^{-2} for V. The equatorial NORPAX MCM data also yields $\widehat{U^{*2}} > \widehat{V^{*2}}$ (Lukas 1987). The magnitude of the zonal current variance maximum

is similar to Hansen and Paul's (1984) maximum values at 30 m, but the meridional structures are completely different. On the other hand, Hansen and Paul's $\widehat{V^{*2}}$ values are stronger than at 30 m in Fig. 28 by a factor of 5, but the meridional structures are similar. The numerical calculation of Philander et al. (1986) also predicts meridional velocity variances which are greater than the zonal velocity variances at 154°W (W. Hurlin, private communication 1987), in contradiction to Figs. 27a and 28a.

Despite the weakened kinetic energy production previously found in B (Fig. 25), $\widehat{U^{*2}}$ in B is only slightly reduced from A near the equator and $\widehat{V^{*2}}$ is actually greater. The implication is that energy from the equatorial front instability propagates south, consistent with the meridional divergence of eddy pressure work discussed in the previous section, or that there are external energy sources, or that there are sources of energy from the production terms that can't be estimated with the ADCP dataset. An additional strong variance peak in the zonal current has arisen at 70–100 m in the NECC, possibly in response to the eddy potential energy production occurring at 4°–6°N and at 7°–8°N which was discussed in the previous section.

Finally, in C a clear peak in the meridional current variance arises at 7°N (Fig. 28c), presumably associated with the eddy potential energy production there. Whether the strong zonal current variance peak at 4°N (Fig. 27c) is associated with this NECC instability or is due to some other equatorial phenomenon is not known. Similarly, the origins of the weaker zonal current variance peak at 2°S, and the weaker meridional current variance peak at 1°–2°N, are not known. We have certainly not identified all the sources of energy for the mesoscale variability in the NORPAX longitude band. But it is probably not simply coincidental that the eddy variances move northward during time periods A, B, and C in concert with the northward movement of the eddy energy production shown in Figs. 25a, 26b, and 26c.

7. Summary

a. Mean-to-eddy kinetic energy production

We have observed a remarkable picture of the spatial and temporal structure of mean-to-eddy energy production. Table 2 summarizes the eddy energy production/loss rates averaged in depth and over three latitude bands that roughly demarcate the regions of the separate instabilities previously discussed. Estimates are presented in Table 2 for the entire time period of the dataset and for time periods A (boreal summer/fall), B (winter), and C (spring). Those production/loss rate estimates that differ from zero by at least one rms error have been *underlined.* The major contributor to the eddy kinetic energy production is $-\rho_* \overline{U^*V^*}(\partial \bar{U}/\partial y)$, which has a maximum at 2°N (Fig. 13) that is significant at 1.8 rms errors, while the total areal average in Table 2a is only slightly less significant. As expected, this term is largest in summer/fall, consistent with prior observations of the seasonal modulation of the mesoscale eddies; but the winter estimate (line 5, column B, in Table 2a) may be low due to the artificial bottom (at 117 m) of our observational domain (Fig. 25b suggests substantial energy production below 117 m at 0°–3°N). The EUC appears to be completely involved in the production of eddy kinetic energy. In fact, the data suggest that significant eddy kinetic energy production exists only when both a westward SECN and an eastward EUC are well developed. This is simply a statement that the barotropic eddy energy production, as it was observed, depends first on the lateral shear between the SECN and EUC. Without the EUC, the shear on the south side of the SECN should be much weaker than that on the north side (e.g., Fig. 21b at the surface).

Consequently, a strong SECN without an EUC could result in an instability arising from the SECN–NECC shear, as originally envisioned by Philander (1976, 1978). There is only a slight indication that the shear on the north side of the SECN is involved in the instability (i.e., Fig. 25a at 3°–4°N) when the EUC is present, although we certainly can't rule out this possibility at other longitudes. [N.B., Hansen and Paul (1984) found only small eddy kinetic energy production in the SECN–NECC shear at 100°–130°W, obtaining roughly equal contributions from the two kinetic energy production terms in lines 5 and 6 of Table 2.] In the mean flow energy conservation equation, we find that the loss of mean flow kinetic energy due to the eddies is substantial for both the EUC and SECN; we will present these results in detail in a subsequent paper.

Production of eddy kinetic energy by $-\rho_* \overline{V^*V^*} \times (\partial \bar{V}/\partial y)$ is insignificant near the equator (line 6 in Table 2a), although possibly enhancing eddy generation during the winter. However, just to the north in the 3°–6°N band (line 6 in Table 2b), the eddies lose energy via this term. In general, this production term does not appear to be very important at 150°–158°W.

Even discounting some large, questionable equatorial estimates in Hansen and Paul (1984), their data suggest that, within a few degrees of the equator, both of the eddy kinetic energy production terms above were stronger at 100°–130°W than we have observed at 150°–158°W for the same time period of summer/fall, 1979 (for instance, compare their Fig. 8 with our Fig. 25a). This longitudinal dependence of the eddy kinetic energy production is not a surprise given previous numerical simulations (e.g., Cox 1980; Philander et al. 1986).

TABLE 2. The area-averaged eddy energetics for three latitude bands encompassing the three observed instabilities. Units are erg cm^{-3} for lines 1–4 or else erg cm^{-3} s^{-1}, and rms errors are shown. The numbers in the Total column are averages over the entire dataset, while numbers in the A, B, and C columns are averages over smaller time periods defined in section 6 of the text: A corresponds to boreal summer/fall 1979; B to winter 1979–80; and C to spring 1980. The Total averages are not simple averages of the respective estimates for the individual time periods because (i) the time periods have varying length, (ii) the time periods do not cover the entire dataset, and (iii) the degrees of freedom for the seasonal estimates have not been reduced for the degrees of freedom lost in the MLR fit, since the seasonal estimates depend on both quantities that have and haven't had the low-frequency variability removed (i.e., for the seasonal estimates, p was set to zero in Table B2). Estimates of energy equation terms that differ from zero by at least one rms error are in italics.

	Total	A	B	C
(a) Average eddy energies and mean-to-eddy energy production, 1°S–3°N				
1. $\frac{1}{2}\rho_* \overline{U^{*2}}$	349 ± 54	334 ± 77	292 ± 69	231 ± 67
2. $\frac{1}{2}\rho_* \overline{V^{*2}}$	223 ± 34	135 ± 30	291 ± 69	103 ± 30
3. $\overline{KE^*}$	572 ± 64	469 ± 83	583 ± 98	334 ± 73
4. $\overline{PE^*}$	294 ± 45	297 ± 66	128 ± 30	233 ± 67
5. $-\rho_* \overline{U^*V^*}(\partial/\partial y)\bar{U}$	*234 ± 161*	*422 ± 275*	112 ± 188	−81 ± 132
6. $-\rho_* \overline{V^*V^*}(\partial/\partial y)\bar{V}$	25 ± 80	−21 ± 80	101 ± 159	13 ± 79
7. $-C\rho^*V^*(\partial/\partial y)\bar{\rho}$	−5 ± 81	−54 ± 130	−8 ± 85	17 ± 110
8. 5 + 6 + 7	*254 ± 197*	*347 ± 315*	205 ± 260	−51 ± 189
(b) Average eddy energies and mean-to-eddy energy production, 3°–6°N				
1. $\frac{1}{2}\rho_* \overline{U^{*2}}$	279 ± 43	120 ± 27	243 ± 57	425 ± 123
2. $\frac{1}{2}\rho_* \overline{V^{*2}}$	177 ± 27	101 ± 23	210 ± 49	136 ± 39
3. $\overline{KE^*}$	456 ± 51	220 ± 35	453 ± 75	561 ± 129
4. $\overline{PE^*}$	402 ± 62	246 ± 55	369 ± 93	310 ± 89
5. $-\rho_* \overline{U^*V^*}(\partial/\partial y)\bar{U}$	20 ± 96	41 ± 90	−120 ± 208	−38 ± 126
6. $-\rho_* \overline{V^*V^*}(\partial/\partial y)\bar{V}$	*−73 ± 65*	*−73 ± 52*	−72 ± 161	−38 ± 79
7. $-C\rho^*V^*(\partial/\partial y)\bar{\rho}$	*119 ± 107*	94 ± 123	*272 ± 214*	125 ± 191
8. 5 + 6 + 7	66 ± 158	62 ± 161	80 ± 339	49 ± 242
(c) Average eddy energies and mean-to-eddy energy production, 6°–10°N				
1. $\frac{1}{2}\rho_* \overline{U^{*2}}$	156 ± 24	78 ± 17	199 ± 47	85 ± 25
2. $\frac{1}{2}\rho_* \overline{V^{*2}}$	95 ± 15	54 ± 12	59 ± 14	120 ± 35
3. $\overline{KE^*}$	251 ± 28	132 ± 21	258 ± 49	206 ± 43
4. $\overline{PE^*}$	278 ± 43	198 ± 44	243 ± 57	198 ± 57
5. $-\rho_* \overline{U^*V^*}(\partial/\partial y)\bar{U}$	−36 ± 50	−13 ± 56	−15 ± 88	*−158 ± 80*
6. $-\rho_* \overline{V^*V^*}(\partial/\partial y)\bar{V}$	−3 ± 28	5 ± 39	−17 ± 32	−4 ± 79
7. $-C\rho^*V^*(\partial/\partial y)\bar{\rho}$	91 ± 111	−73 ± 111	63 ± 104	277 ± 322
8. 5 + 6 + 7	52 ± 125	−81 ± 130	31 ± 140	115 ± 341

The comparison of our observed Reynolds stresses (Fig. 23a) with Philander et al.'s (1986, Figs. 5 and 6) numerical values implies that the appropriate level of parametric dissipation for their model is obtained with a horizontal eddy viscosity $A_H = 1 \times 10^7$ cm^2 s^{-1} or less, and certainly not with $A_H = 2 \times 10^{-7}$ cm^2 s^{-1}. However, the model is forced with Hellerman and Rosenstein's (1983) climatological mean winds that are stronger at 150°–158°W near the equator than the observed winds during 1979 (Wylie et al. 1984). Hence, an even smaller value of A_H may be appropriate if $\overline{U^*V^*}$ is positively correlated with the magnitude of the wind forcing. It is now reasonable to wonder whether further model-data comparisons will find that the same level of dissipation as that found appropriate for the model at 150°–158°W is appropriate at other longitudes.

b. Mean-to-eddy potential energy production

Within 3° of the equator at 150°–158°W, conversion of mean-to-eddy potential energy is weak (line 7 in Table 2a), in contrast to the large values found by Hansen and Paul (1984) at 100°–130°W. This indicates a second change in the character of the near-equatorial instability as a function of longitude. Considering that we did find substantial eddy potential energy production at the equatorial front (Fig. 26b, and line 7, column B, of Table 2b), the longitudinal difference could simply be ascribed to variations in the latitude and strength of the equatorial front, since it is stronger and closer to the equator at 100°–130°W. However, this explanation belittles the fact that the near-equatorial instability and the equatorial front instability are distinctly separate phenomena at 150°–

158°W since they are strongest at different times of the year.

A surprising result of this study is the discovery of eddy potential energy production in the NECC thermocline. This phenomenon is clearly distinct from the instabilities near the equator and at the equatorial front, because it is strongest in spring (line 7 in Table 2c) rather than in summer/fall or winter as for the other two instabilities, respectively. Since most of the features associated with this phenomenon (such as peak estimates and areal averages of density flux and eddy potential energy production) are significant at only around one rms error, the proposition that the NECC is baroclinically unstable is only that, a proposition. The eddy variances associated with the region of eddy potential energy production suggest that the fluctuations are confined to a small latitude–depth range: that is, they are trapped to the production region, as expected for fluctuations produced by an instability of an eastward jet (Talley 1983).

While the eddy potential energy production at 6°–10°N during the spring averages $277 \pm 322 \times 10^{-6}$ ergs cm^{-3} s^{-1}, the eddy kinetic energy production at the same time in the same region (line 5, column C in Table 2c) averages $-158 \pm 80 \times 10^{-6}$ ergs cm^{-3} s^{-1}. That is, the eddies appear to gain potential energy from the available mean potential energy while at the same time they lose a large amount of kinetic energy to the mean flow. Note too that the equatorial front instability also behaves in this manner (lines 5 and 7, column B, Table 2b). Similar energy transfers have been found in the Gulf Stream recirculation region (Bryden 1982) and in the atmosphere, and are common in numerical models (Wood 1988). For baroclinically unstable but barotropically stable zonal jets, Talley (1983) showed theoretically that eddies gain potential energy from the available mean potential energy field but lose kinetic energy to the mean currents.

The NECC instability may occur due to the presence of the Line Islands ridge upstream (west) of our observation region (Palmyra Island is at 6°N, 162°W). Consequently, the NECC eddies may exist for only a relatively short distance downstream of the Line Islands. Hogg (1983) has noted that the New England Seamount Chain appears to greatly intensify the instability of the Gulf Stream.

The dominant periods of the NECC eddies cannot be determined with the ADCP data. Far to the east, at 110°W, Inverted Echo Sounder observations (Miller et al. 1985) during 1980–81 showed longer period variability at 9°N (60 day period) than closer to the equator (30–40 day period). Whether the variability at 9°N, 110°W has an energy source similar to that observed in the NECC thermocline at 150°–158°W isn't known. Certainly, it seems prudent to expect that the ocean has additional undiscovered energy sources for mesoscale variability. The westward North Equatorial Current, just to the north of the NECC, must certainly be a candidate for instability, since westward currents are inherently more unstable than eastward currents (e.g., Pedlosky 1964).

c. *Low-frequency–to–eddy energy production*

Table 3 summarizes the areal averages of eddy energy production due to interaction with the low-frequency or annual cycle (1 and 2 cpy) variability. Nowhere is the conversion of low-frequency–to–eddy energy large or significant. The various conversion terms tend to cancel so that their sum in each latitude band is even less significant. Near the equator the eddies lose kinetic energy to the annual cycle (line 9, Table 3), although this is significant at no more than 1.4 rms errors even in the unaveraged results (i.e., Fig. 15). Rather than losing energy, one would expect the eddies to gain kinetic energy from the annual cycle, since (1) the eddy kinetic energy production (specifically $-\rho_* \widehat{U^*V^*}(\partial\hat{U}/\partial y)$ has a large annual cycle in amplitude (see Table 2a), and (2) this energy production is strongest in summer/fall when the zonal currents have their largest meridional shears due to enhancement by the annual cycle. However, $\widetilde{U^*V^*}$ and $\partial\tilde{U}/\partial y$ are not generally in phase, partly because $\tilde{U}$ has a strong southward phase propagation (Johnson 1987) and partly because $\widetilde{U^*V^*}$ doesn't reach its positive maximum until well after the negative maximum of $\partial\tilde{U}/\partial y$.

In other words, the equatorial instability is enhanced, possibly even triggered, by the annual cycle shear, but the eddy kinetic energy production continues for many months even as $\partial\tilde{U}/\partial y$ approaches zero and changes sign, causing a decrease in the magnitude of $\partial\hat{U}/\partial y$. Whether the annual cycle of zonal currents act to trigger the instability, or whether the mean currents are generally unstable and the annual cycle turns off the instability for part of the year, is unclear. Given that a necessary condition for barotropic instability at midlatitudes (zero crossings in the gradient of absolute vorticity) is satisfied by the mean zonal currents, as

TABLE 3. Average low-frequency–to–eddy energy production. See caption to Table 2.

	Total		
	1°S–3°N	3°–6°N	6°–10°N
9. $-\rho_*\overline{\widetilde{U^*V^*}(\partial/\partial y)\tilde{U}}$	−61 ± 77	−47 ± 51	−1 ± 22
10. $-\rho_*\overline{\widetilde{V^*V^*}(\partial/\partial y)\tilde{V}}$	29 ± 52	5 ± 48	0 ± 20
11. $-C\overline{\rho^*\widetilde{V^*}(\partial/\partial y)\tilde{\rho}}$	−4 ± 43	51 ± 66	−26 ± 49
12. 9 + 10 + 11	−36 ± 102	9 ± 96	−27 ± 57
13. 8 + 12	218 ± 222	75 ± 185	25 ± 137

noted in the Introduction, and that the eddies lose energy to the annual cycle on average, we believe that the important role of the annual cycle at 150°–158°W is to weaken the mean shear sufficiently for a few months each year so that the instability stops. In the Atlantic Ocean, where a similar instability exists for only a few months each year (Weisberg and Weingartner 1988), the annual cycle must be considered to have a more constructive role in producing the instability.

As a matter of curiosity, the energy conversions between the low-frequencies and the eddies at 3°–6°N follow the same pattern as the mean to eddy energy conversions; that is, the eddies gain potential energy and lose kinetic energy (Table 3, second column). However, the average conversion rates are not significant at even one rms error.

d. Advection and diffusion

The areal averages of the various components of the kinetic and potential energy advection divergence can be found in Table 4 (lines 14–16 and 19–21). In general, the estimates are not large or significant at even 1 rms error. In addition, the estimates tend to cancel so that the sums of all the divergence terms in each latitude band are quite small, further evidence of the minor importance of advection divergence to the total energy budgets of the eddies. Locally, however, redistribution of energy by advection may play a small role in the energy budgets (e.g., Fig. 18).

The diffusion of eddy kinetic energy represented by the average meridional divergence of eddy pressure work (line 17 in Table 4) has rather large values in each latitude band, but is significant in the areal averages only near the equator. The sign of the latter estimates is such that the eddies are gaining energy from this term; that is, rather than radiating energy away meridionally, the eddies are absorbing energy from this direction near the equator in the 150°–158°W longitude band.

TABLE 4. Eddy energy advection and diffusion. See caption to Table 2.

	Total		
	1°S–3°N	3°–6°N	6°–10°N
14. $-\bar{V}(\partial/\partial y)\overline{KE^*}$	10 ± 48	17 ± 41	8 ± 22
15. $-\bar{V}(\partial/\partial y)\widetilde{KE^*}$	−6 ± 82	0 ± 75	−15 ± 31
16. $-\overline{V^*(\partial/\partial y)KE^*}$	90 ± 113	−22 ± 124	22 ± 43
17. $-\overline{V^*(\partial/\partial y)P^*}$	*771 ± 423*	−265 ± 458	265 ± 325
18. 14 + 15 + 16 + 17	*865 ± 448*	−270 ± 482	280 ± 330
19. $-C\bar{V}(\partial/\partial y)\rho^{*2}$	−11 ± 33	−24 ± 66	−15 ± 37
20. $-C\bar{V}(\partial/\partial y)\widetilde{\rho^{*2}}$	50 ± 51	−5 ± 78	18 ± 46
21. $-C\overline{V^*(\partial/\partial y)\rho^{*2}}$	−21 ± 35	*50 ± 47*	−43 ± 118
22. 19 + 20 + 21	*−82 ± 70*	21 ± 112	−40 ± 132
23. 18 + 22	*783 ± 453*	−249 ± 495	240 ± 355
24. 23 + 13	*1001 ± 504*	−174 ± 528	265 ± 381

e. Energy sums and missing terms

The sum for each latitude band of all the terms on the right hand side of Eqs. (3.3) and (3.5) is given on line 24 of Table 4. Each of the three estimates is dominated by the meridional divergence of eddy pressure work, but north of 3°N the areal averages are not significant. The equatorial estimate, though, is significant at 2 rms errors, being about 75% due to eddy pressure work divergence and about 25% due to eddy kinetic energy production. It is not likely that the large imbalance of the total eddy energy equation indicated by the equatorial sum is due to an increasing eddy energy level at the equator, but rather that our dissipationless assumption is incorrect, or that some of the terms in the full energy Eqs. (3.2 and 3.4) that were neglected are important. The most obvious candidates are the zonal and vertical eddy pressure work divergences. Weisberg and Weingartner (1988) found the former to be of opposite sign and nearly equal magnitude to the meridional pressure work divergence in the western equatorial Atlantic, while the latter was small. The production of eddy energy through the working of mean shears on the zonal, $\overline{U^{*2}}$, and vertical, $\overline{U^*V^*}$, Reynolds stresses also has been found to be relatively unimportant in the Atlantic (Weisberg and Weingartner 1988). However, Brady (1990) finds $-\rho_* \overline{U^*W^*}(\partial\bar{U}/\partial z)$ to be comparable in magnitude, but of opposite sign, to $-\rho_* \overline{U^*V^*}(\partial\bar{U}/\partial y)$ at the equator at 110°W. (Both Brady 1990 and Weisberg and Weingartner 1988 inferred $\overline{U^*W^*}$ or W^* indirectly, but with different methods.) While in the future we will relax our zonal invariance assumption and attempt estimates of those eddy energy production, advection and diffusion terms that depend on zonal gradients, the ADCP data appears to be too temporally and spatially sparse to permit plausible estimation of W^*. Estimation of downward radiation of energy, represented by the vertical eddy pressure work divergence, is therefore also prohibited, despite the probable importance of this term in the upper ocean eddy energetics in the Pacific (Cox 1980).

8. Caveats and comments

a. The representativeness of 1979–80

Proper interpretation of the present work depends on whether the phenomena we have observed are typical year after year at these longitudes. If 1979–80 were unusual for some reason, then the results presented here would not be generally applicable to other years, but would at least describe one of the possibly many states that can exist in the Pacific Ocean. The Legeckis et al. (1983) satellite observations of the now classic SST cusp pattern seem to suggest weaker than usual

eddy activity in 1979. However, Hansen and Paul (1984) point out that their drifter observations show strong eddy activity farther to the west and later in the year than is shown by Legeckis et al., demonstrating that SST may not be a faithful indicator of eddy activity. The latitude–time plots of dynamic height, salinity, and surface geostrophic velocity presented by Kessler and Taft (1987) suggest that the large-scale flows in 1979–80 were fairly normal, except that the NECC failed to reach as large an annual maximum transport in December 1979 through February 1980 as it did in the prior or subsequent winters. Aside from this feature, the annual cycle during the Shuttle Experiment is considered fairly normal (see Lukas and Firing 1985 for a discussion of the winds, and Johnson 1987 for a discussion of dynamic height). The mean zonal winds for 1979 within a few degrees of the equator were slightly weaker (Wylie et al. 1984) than the long term mean (Wyrtki and Meyers 1975), while indices of the central tropical Pacific trade winds were quite normal during the 1979–80 Shuttle Experiment (Kousky 1989). Stronger mean zonal winds in other years should produce increased shear between the SECN and EUC, and therefore stronger eddy energy production near the equator. This may partially explain why the eddy variability on the equator during 1979–80 (e.g., Fig. 1) is weaker than that found at the equator at 140°W in 1983–85 (Halpern et al. 1988). Of course, we've already noted that the eddy kinetic energy production between 0° and 2°N increases to the east of 150°W, even in 1979.

b. *The episodic nature of heat flux*

Estimates of eddy heat flux, $\overline{V^*T^*}$, and similarly eddy density flux, $\overline{V^*\rho^*}$, from both ADCP and drifter observations may be subject to unexpected biases. Luther et al. (1987) have found that at 3°S, 140°W, the near-surface eddy heat flux appears to be highly episodic, being concentrated in 1 to 2 week time periods. These episodes appear to be due to cold water filaments that form occasionally as a non-linear amplification on the southward edges of the mesoscale eddies in the region. The irregular spacing of the ADCP sections, combined with the episodic nature of the eddy heat flux, suggests that the sections could easily have missed one or more episodes. Alternatively, the episodes could have been oversampled. The sign of the resulting error is indeterminate, but at least the error can be reduced during future experiments by increasing the sampling rate or increasing the duration of the data collection.

For drifters, however, both Niiler (1986, private communication) and Luther (1988, private communication) note that the filaments of cold water appear to be associated with convergent flow that could easily entrain any drifter in the vicinity, resulting in an overall bias toward higher equatorward heat flux than exists on average. In fact, Niiler has noted just such an entrainment of several drifters that were deployed on the equator at different longitudes. Due to the convergent flow in the filaments, the bias in the drifter heat flux estimates cannot be easily mitigated by the deployment of more drifters.

It is not known whether eddy heat flux north of the equator will be similarly episodic. The near-surface meridional shear of the zonal currents is much stronger north of the equator and therefore the type of cold water filament observed south of the equator is likely to be rapidly distorted as, and if, it begins to from north of the equator.

c. *The value of ADCP observations*

This and other recent papers (e.g., Wilson and Leetmaa 1988) further demonstrate the substantial value of shipborne ADCP observations, especially in conjunction with concurrent density or temperature measurements. While there are drawbacks to the ADCP data, such as the lack of information on the frequency content of the fluctuations, these are not vexing for certain important applications, such as determining the interaction of the fluctuations with the mean and low-frequency flows and estimating the energetic balances of the fluctuations. The lack of frequency information is even less important in studies of the mean and low-frequency flow energetics and fluxes, which are the subjects of future papers. For the case where an interesting eddy–mean flow interaction is discovered through ADCP observations, subsequent experiments with current meter moorings, or other rapid samplers, can be fielded to ascertain the eddy spectral characteristics.

In order for studies such as this to be undertaken successfully, repeated sections are required in sufficient number to adequately define the means (and therefore the fluctuation amplitudes). The upcoming WOCE could benefit greatly from having repeated sections of ADCP observations, along with temperature or density observations, along selected tracks throughout the oceans. Plans for such data collection are being formulated, although not by the present authors.

Acknowledgments. The extensive efforts of Drs. Regier, Knox and Cutchin in deploying and shepherding the ADCP during the Shuttle Experiment are gratefully acknowledged. This work was supported at SIO by NSF Grants OCE87-00462 and OCE88-17706.

APPENDIX A

Data Processing

1. ADCP data

The ADCP used was developed by AMETEK/Straza. It is an improved version of the modified ship's log employed by Regier (1982a). It transmits 20 ms

pulses of 300 kHz sound along four narrow beams. The beams angle down into the water at 60° from the horizontal in four directions: forward, aft, to port, and to starboard of the ship. Sound reflected back to the instrument from supposedly passively drifting scatterers in each beam experiences a Doppler shift, which is proportional to the water velocity along the beam relative to the instrument. The Doppler shifts of the forward and aft beams are differenced to give a number proportional to the forward component of horizontal water velocity relative to the ship; the vertical velocity cancels in the differences. Likewise, the port and starboard beams give the athwartships velocity. Velocities are calculated for 32 depth bins 6.5 m apart with the shallowest at 13 m. The bins are about 13 m wide, so only every second bin is independently measured. The instrument evaluates the quality of each return echo as a function of depth and rejects unusable depth bins. The usable data is block averaged over 500 pings (about 5 minutes, or 1.5 km at a ship speed of 10 kt) to reduce both the data volume and the random ping-to ping noise of about 10 cm s^{-1} (Regier 1982b). For the analyses presented here, data from bins below 117 m has not been employed, because it often appeared noisy and had low (less than 50%) numbers of valid returns.

The relative velocity profiles are rotated into geographical coordinates using the ship's heading recorded automatically every two minutes. Gaps in this heading time series are filled using the ship's bridge log; when underway the ship's course was so steady that these log entries are almost as accurate as the recorded headings. When the ship was on station the logged headings were unusable: so in the absence of automatically recorded headings, the ship was assumed to be stationary with respect to the water at 26 m depth. This resulted in increased noise in the velocity profiles taken while the ship was on station. In addition, such profiles were often contaminated by heading changes during the 500 ping averaging period.

Knowledge of the ship's velocity relative to the earth allows the rotated ADCP relative velocities to be converted to absolute velocities. The ship's velocity is found from sequential TRANSIT satellite fixes recorded by the ship's computer. The absolute water velocity is then

$$\mathbf{V}_w = \frac{1}{t_2 - t_1}\left[\mathbf{X}_2 - \mathbf{X}_1 + \int_{t_1}^{t_2} \mathbf{V}_r dt\right]$$

where $\mathbf{V}_w$ and $\mathbf{V}_r$ are the absolute and relative water velocities, respectively, and $\mathbf{X}_n$ is the ship's position at t_n. $\mathbf{V}_w$ is known only as an average between adjacent fixes, which are typically around 1.5–2 h and 30–40 km apart; therefore absolute velocities are known only over relatively large scales.

The ADCP data has been cleaned and corrected for a number of errors (see Johnson et al. 1988; Johnson 1987, for details). Bit drops included in the digitally recorded data were corrected, data subject to problems with the instrument's data quality control were eliminated, and all the data was corrected for variations in sound speed using nearby CTD data. Unrecoverable errors in the data due to ship motion (i.e., roll and heave) were small during the experiment. The heading data was corrected in one section for a 5° offset noted by shipboard personnel. The remaining heading bias is estimated to yield a 5 cm s^{-1} zonal current bias (positive for a northward track) with a standard error of 1.5 cm s^{-1} (Johnson et al. 1988). At a speed of 10 kt, this bias corresponds to a heading error of −0.56°, or more probably a transducer misalignment of +0.56°. Since the ship's track (Fig. 2) was traversed in alternate directions, the heading bias should have little effect on the mean currents. This bias contributes about 4% of the observed variance. Satellite fixes were examined subjectively and about 13% were eliminated (Johnson 1987). Such eliminations result only in longer averaging intervals for $\mathbf{V}_w$ above. Regier (1982b) estimates the rms velocity error from the satellite fixes to be 4 cm s^{-1} for a fix spacing of two hours (~40 km at a ship speed of 10 kt). This error increases (decreases) with shorter (longer) time intervals between fixes.

For this study, the absolute velocities along each section have been averaged into 1° latitude bins centered on integral latitudes. This reduces the navigational noise and provides a one-to-one correspondence between the ADCP and CTD data. Velocities measured while the ship was on station have been generally excluded from the analysis in an effort to reduce noise due to ship drift while on station. However, due to the spatial averaging required by the satellite navigation method, some information from velocities taken on station is included in the 1° averages, as well as some information from velocities outside the boundaries of the 1° average. The range of the data is restricted to 4°S–10°N in order to obtain uniform coverage at each of the sampling longitudes (Fig. 2) and to maximize the amount of data at each latitude to be studied. Data below 117 m is not used due to the poor quality mentioned above, and velocities above 26 m are rejected as biased in the direction of the ship's motion (Johnson et al. 1988). The 27 sections retained for analysis average 95% complete.

2. CTD data

The CTD stations at integral latitudes produced temperatures and salinities every 2.5 m in depth to over 1000 m (Williams 1980–81). We use the reported in situ temperature and potential density trapezoidally integrated over the depth bins of the ADCP data. Only the 27 sections concurrent with the ADCP sections are used here. No attempt has been made to match holes within the datasets by deleting data within the sections, so there is not an exact one-to-one correspondence between the two sets. XBT data exist at the half-degrees between the CTD data, but they are so biased and noisy

relative to the CTD data that we were unable to incorporate them into this analysis.

Pressures were calculated by integrating the hydrostatic equation, using the multiple linear regression function and residuals (see section 3b) of potential density, from 988 m depth to the standard depths of the analysis. The regression was performed on the densities prior to integration only so that the large mean and the small fluctuations would be numerically independent throughout the integration.

APPENDIX B

Error Analysis

Due to our incomplete knowledge of the probability density functions of the oceanic variables, we must make assumptions about those functions in order to calculate the errors of our statistical estimates. Our primary assumption is that all the variables are joint-normally distributed (JND). Tests for JND involve the higher statistical moments of the distribution, i.e., skewness ($\langle x^3\rangle/\langle x^2\rangle^{2/3}$) and kurtosis ($\langle x^4\rangle/\langle x^2\rangle^2$), which are not well observed with the present datasets. The skewness and kurtosis of U^*, V^*, and ρ^* show no significant departures from those of normal distributions. We also tested the joint normality of all pairs of these variables by calculating the quantity

$$Q = \langle x^2y^2\rangle - [\langle x^2\rangle\langle y^2\rangle + 2\langle xy\rangle^2]$$

which vanishes for JND variables. Again we found no significant departures from JND.

Lukas (1987) tested the product U^*V^* for skewness using high-frequency velocities from the concurrent NORPAX MCM data. He finds large positive skewness at all instrument locations. This does not imply that U and V are not JND. For U and V JND, the skewness of the product UV about the mean $\langle UV\rangle$ is

$$\alpha_3 = \frac{6\langle U^2\rangle\langle V^2\rangle\langle UV\rangle + 4\langle UV\rangle^3}{(\langle U^2\rangle\langle V^2\rangle + \langle UV\rangle^2)^{3/2}} \quad \text{(B1)}$$

where $\langle\ \rangle$ denotes the expectation value, as compared to the sample mean, ($\bar{}$). The right hand side of (B1) is nonzero for all nonzero covariances. Table B1 compares Lukas' UV skewness with values from (B1) calculated using Lukas' variances and covariances from the same instruments. Lukas' estimates are smaller than α_3 at the top two depths and larger below. The overall means of the skewness estimates in Table B1 are 1.17/0.93. The uncertainty in the estimation of α_3 is large, so that the skewness comparisons are not sensitive tests of JND. But there is certainly not such strong disagreement that JND should be rejected as the lowest order model for the probability distribution of the data. In light of the results from all the tests noted above, the data are assumed to be JND for the purpose of calculating rms errors.

TABLE B1. The NORPAX moored current meter estimates by Lukas (1987) of the skewness of U^*V^* compared to the expected skewness for joint normally distributed variables U and V having the estimated variances given by Lukas.

Depth	0°40'S	0°	0°40'N
15 m	—	—	1.20/1.76
50 m	—	0.98/1.46	—
100 m	0.68/0.10	1.46/0.80	1.40/0.77
150 m	—	—	1.27/0.70

Our second assumption is that the statistics are stationary. While probably true over several months, this is obviously not true for the whole year of data; the instabilities have substantial seasonal dependences. Averaging an energetic period with an unenergetic period dilutes the variances and covariances of the instability. Since variance varies as n^{-1} (where n is the number of observations) and error limits vary as $n^{-1/2}$, averaging over the year tends to diminish the nonstationary variances more than the error limits. Hence, nonstationary quantities which are significant in the yearly average will have preserved or enhanced significance in a more time limited average. Therefore, our error estimates will tend to be conservative due to the assumption of stationarity. The high-frequency fields will have nonstationary statistics if significant amounts of variance are contributed by lower frequency background flow variability. We have removed annual and semiannual harmonics from the flows, and have concluded in section 3b that interannual variability is small for the NORPAX time period. Therefore, the high-frequency residuals should be free of significant low-frequency variability.

The last assumption is that the high-frequency sections are independent in time. This is demonstrated by the fact that the time lagged autocovariance functions fall to near-zero or less at the shortest lags observed (about 3 days) for all flow variables at all latitudes. Figure B1 shows the time lagged covariance of U^* and V^* averaged over all latitudes.

The errors presented in the body of the paper are the rms errors of the estimate. Our rms errors are also standard errors since our bias error is zero; all of our estimators are unbiased. Since the estimates are approximately normally distributed, 95% confidence limits extend 1.96 rms errors from the estimate, while 90% confidence limits extend 1.65 rms errors and 80% confidence limits extend 1.28 rms errors. For all estimates of the variability the degrees of freedom are reduced by 5 to account for variance absorbed into the MLR (section 3b), which fits five functions to the data. With the assumptions stated above, the rms errors of the basic statistical estimates are as shown in Table B2. In all cases the data used are the high-frequency fields, except in the estimation of the "mean" where the total field is used. For computational ease we use the alter-

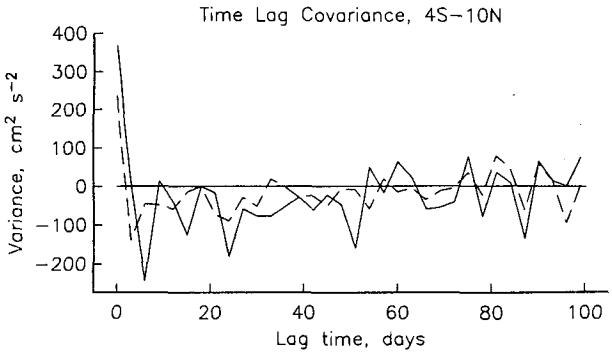

FIG. B1. The time lagged autocovariance of eddy velocity at each latitude and depth, averaged over all latitudes and depths. The solid line is zonal velocity covariance, the dashed, meridional. The lagged-covariances are time averaged into three day bins, such that the 0 day bin contains lags from 0 to 1.5 days, the 3 day bin contains lags from 1.5 to 4.5 days, etc. The smallest nonzero lags available correspond to pairs of sections taken 4 days apart. Note that the lagged covariance drops to zero by the first (3 day) lag, implying that the sections are independent in time.

native form for errors of $\overline{XY}$ and the analogous form for errors of $\partial\overline{XY}/\partial y$ (as shown).

The errors of products of the basic statistics are built up from the errors of those statistics. For JND variables the variance of a product about the mean product is

$$\langle (xy - \langle xy\rangle)^2\rangle = \langle x\rangle^2\sigma_y^2 + \langle y\rangle^2\sigma_x^2 + 2\langle x\rangle\langle y\rangle C_{xy} + \sigma_x^2\sigma_y^2 + C_{xy}^2 \quad \text{(B2)}$$

where σ^2 and C denote variances and covariances, respectively. The variance of a product about the product of the means is one C_{xy}^2 greater than the right hand side of (B2). Covariances are not JND, so (B2) does not apply exactly to products involving covariances, such as the energy production terms. Products of covariances of JND variables with means of JND variables have variance

$$\langle \overline{xy}\bar{z} - \langle xy\rangle\langle z\rangle)^2\rangle = \langle\overline{xy}\rangle^2\sigma_{\bar{z}}^2 + \langle\bar{z}\rangle^2\sigma_{\overline{xy}}^2 + \sigma_{\overline{xy}}^2\sigma_{\bar{z}}^2. \quad \text{(B3)}$$

The covariances which appear in (B2) do not appear in (B3) since the mean product of 3 JND variables is zero. Errors of mean and turbulent energy production estimates are built from the error estimates of Table B2 using (B3). For potential energy production estimates the errors of $[\partial(\rho_0 + \bar{\rho})/\partial z]$ are neglected; they are only about 20% of the mean values.

All the error estimates used in this study require exact knowledge of variances, covariances, etc., while in actuality, estimates from the data are employed. The error estimates would probably be larger if the uncertainties in the components of the error estimators were taken into account; the simplest analogue is the relationship between the student t distribution and the Normal distribution which are used to estimate confidence intervals for the means of observations of random variables with unknown and known variances, respectively. Incorporating component uncertainties into the error estimators goes well beyond the scope and needs of the present work.

Throughout the paper we test the significance of estimated quantities (i.e., whether they are distinguished from zero) by determining whether they are 1–2 rms errors from zero. This is a conservative approximation in the case of covariances: a more exact test of the null hypothesis would be to assume that the true covariance is zero, recalculate the rms errors (using the first covariance error formula in Table B2), and inquire whether the estimate is more than two adjusted rms errors from zero. This yields enhanced significances in cases where the estimated covariance is a large fraction of the variances; that is, where the correlation is high. For example, $\widehat{V^*\rho^*}$ in the NECC thermocline during time period C can be shown to be significantly different from zero at 2 rms errors (adjusted) even though zero is only 1.1 rms errors (unadjusted) from the estimate.

The net result of all the assumptions noted in this appendix is that the error estimators used in this paper are at once more conservative and more liberal than ideal estimators. The determination of better estimators

TABLE B2. The statistical estimators used for basic quantities and their rms errors. The number of degrees of freedom lost in the MLR are denoted as p.

Term	Estimate	Mean square error
mean	MLR	$\left(\frac{1}{n}\overline{X^2}\right)$
$\overline{X^2}$	$\frac{1}{n-p}\sum X_i^2$	$\frac{2}{n-p}(\overline{X^2})^2$
$\overline{XY}$	$\frac{1}{n-p}\sum X_iY_i$	$\frac{1}{n-p}[\overline{X^2Y^2} + \overline{XY}^2]$
	alternatively,	$\frac{n}{(n-p-1)(n-p)^2}\sum\left[X_iY_i - \frac{1}{n}\sum X_jY_j\right]^2$
$\frac{\partial}{\partial y}\overline{XY}$	$\frac{1}{n-p}\sum\frac{\partial}{\partial y}(X_iY_i)$	$\frac{n}{(n-p-1)(n-p)^2}\sum\left[\frac{\partial}{\partial y}\left(X_iY_i - \frac{1}{n}\sum X_jY_j\right)\right]^2$

is itself a lengthy undertaking which we will not attempt. The estimators are at least consistently applied throughout the paper, which we believe allows accurate judgement of relative importance, if not absolute.

REFERENCES

Brady, E. C., 1990: Observations of equatorial 21-day wave–mean flow interaction at 110°W. Ph.D. thesis, M.I.T.–W.H.O.I. Joint Program.

Bryden, H., 1982: Sources of eddy energy in the Gulf Stream recirculation region. *J. Mar. Res.*, **40**, 1047–1068.

Bryden, H. L., and E. C. Brady, 1989: Eddy momentum and heat fluxes and their effects on the circulation of the equatorial Pacific Ocean. *J. Mar. Res.*, **47**, 55–79.

Chereskin, T. K., D. Halpern and L. A. Regier, 1987: Comparison of shipboard acoustic Doppler current profiler and moored current measurements in the equatorial Pacific. *J. Atmos. Oceanic Technol.*, **4**, 742–747.

Cox, M. D., 1980: Generation and propagation of 30-day waves in a numerical model of the Pacific. *J. Geophys. Res.*, **10**, 1168–1186.

Dewar, W. K., and J. M. Bane, Jr., 1985: Subsurface energetics of the Gulf Stream near the Charleston Bump. *J. Phys. Oceanogr.*, **15**, 1771–1789.

Düing, W., P. Hisard, E. Katz, J. Meincke, L. Miller, K. V. Moroshkin, G. Philander, A. A. Ribnikov, K. Voigt and R. Weisberg, 1975: Meanders and long waves in the equatorial Atlantic. *Nature*, **257**, 280–284.

Eriksen, C. C., 1980: Evidence for a continuous spectrum of equatorial waves in the Indean Ocean. *J. Geophys. Res.*, **85**, 3285–3303.

Fantini, M., and Ka-Kit Tung, 1987: On radiating waves generated from barotropic shear instability of a western boundary current. *J. Phys. Oceanogr.*, **17**, 1304–1308.

Firing, E., C. Fenander and J. Miller, 1981: Profiling current meter measurements from the NOR-PAX Hawaii-to-Tahiti shuttle experiment. Data Rep. 39, HIG-81-2, Hawaii Institute of Geophysics, University of Hawaii, 146 pp.

Firing, E., and R. Lukas, 1985: Sampling and aliasing during the NORPAX Hawaii-to-Tahiti shuttle experiment. *J. Geophys. Res.*, **90**, 11709–11718.

Fu, L.-L., 1981: Observations and models of inertial waves in the deep ocean. *Rev. Geophys. Space Phys.*, **19**, 141–170.

Halpern, D., 1979: Observations of upper ocean currents at DOMES sites A, B, and C in the tropical central North Pacific Ocean during 1975 and 1976. *Marine Geology and Oceanography of the Pacific Manganese Nodule Province*, J. L. Bischoff, D. Z. Piper, Eds. Plenum, 43–82.

Halpern, D., R. A. Knox and D. S. Luther, 1988: Observations of 20-day period meridional current oscillations in the upper ocean along the Pacific equator. *J. Phys. Oceanogr.*, **18**, 1514–1534.

Hansen, D. V., and C. A. Paul, 1984: Genesis and effects of long waves in the equatorial Pacific. *J. Geophys. Res.*, **89**, 10431–10440.

Hellerman, S., and M. Rosenstein, 1983: Normal monthly wind stress over the world ocean with error estimates. *J. Phys. Oceanogr.*, **13**, 1093–1104.

Hendry, R. M., 1977: Observations of the semidiurnal internal tide in the western North Atlantic Ocean. *Phil. Trans. Roy. Soc. London*, **A 286**, 1–24.

Hogg, N., 1983: A note on the deep circulation of the western North Atlantic: Its nature and causes. *Deep-Sea Res.*, **30**, 945–961.

Johnson, E. S., 1987: Studies of Doppler acoustic velocities measured during the NORPAX Hawaii-to-Tahiti Shuttle. Ph.D. dissertation, University of California, San Diego, 103 pp.

——, L. A. Regier and R. A. Knox, 1988: A study of geostrophy in tropical Pacific Ocean currents during the NORPAX Tahiti shuttle using a shipboard Doppler acoustic current profiler. *J. Phys. Oceanogr.*, **18**, 708–723.

Kessler, W. S., and B. A. Taft, 1987: Dynamic heights and zonal geostrophic transports in the central tropical Pacific during 1979–84. *J. Phys. Oceanogr.*, **17**, 97–122.

Kindle, J. C., and J. D. Thompson, 1989: The 26- and 50-day oscillations in the western Indian Ocean: Model results. *J. Phys. Oceanogr.*, **19**, 4721–4736.

Knox, R. A., and D. Halpern, 1982: Long range Kelvin wave propagation of transport variations in Pacific Ocean equatorial currents. *J. Mar. Res.*, **40**(Suppl.), 329–339.

Kousky, V. E., Ed., 1989: *Climate Diagnostics Bulletin.* Climate Analysis Center, NMC, NOAA, Washington, DC.

Legeckis, R., 1977: Long waves in the eastern equatorial Pacific Ocean: A view from a geostationary satellite. *Science*, **197**, 1179–1181.

——, W. Pichel and G. Nesterczuk, 1983: Equatorial long waves in geostationary satellite observations and in a multichannel sea surface temperature analysis. *Bull. Amer. Meteor. Soc.*, **64**, 133–139.

Lukas, R., 1987: Horizontal Reynolds stresses in the central equatorial Pacific. *J. Geophys. Res.*, **92**, 9453–9463.

Lukas, R., and E. Firing, 1984: The geostrophic balance of the Pacific Equatorial Undercurrent. *Deep-Sea Res.*, **31**, 61–66.

——, and ——, 1985: The annual Rossby wave in the central equatorial Pacific Ocean. *J. Phys. Oceanogr.*, **15**, 55–67.

Luther, D. S., and D. E. Harrison, 1984: Observing long-period fluctuations of surface winds in the tropical Pacific: Initial results from island data. *Mon. Wea. Rev.*, **112**, 285–302.

——, E. S. Johnson and R. A. Knox, 1987: Comparisons of observed and modeled eddy statistics from the upper equatorial Pacific Ocean. *Eos*, **68**, 1719.

——, R. A. Knox and D. Halpern, 1987: Eddy heat fluxes in the upper equatorial Pacific Ocean along 140°W. *Eos*, **68**, 1321.

McPhaden, M. J., and B. A. Taft, 1988: On the dynamics of seasonal and intra-seasonal variability in the eastern Equatorial Pacific. *J. Phys. Oceanogr.*, **18**, 1713–1732.

Meyers, G., 1979: Annual variation in the slope of the 14°C isotherm along the equator in the Pacific Ocean. *J. Phys. Oceanogr.*, **9**, 885–891.

Miller, L., D. R. Watts and M. Wimbush, 1985: Oscillations of dynamic topography in the eastern equatorial Pacific. *J. Phys. Oceanogr.*, **15**, 1759–1770.

Munk, W. H., 1980: Internal wave spectra at the buoyant and inertial frequencies. *J. Phys. Oceanogr.*, **10**, 1718–1728.

Pedlosky, J., 1964: The stability of currents in the atmosphere and the ocean, Part I. *J. Atmos. Sci.*, **21**, 201–219.

Philander, S. G. H., 1976: Instabilities of zonal equatorial currents. *J. Geophys. Res.*, **81**, 3725–3735.

——, 1978: Instabilities of zonal equatorial currents, Part 2. *J. Geophys. Res.*, **83**, 3679–3682.

——, W. J. Hurlin and R. C. Pacanowski, 1986: Properties of long equatorial waves in models of the seasonal cycle in the tropical Atlantic and Pacific oceans. *J. Geophys. Res.*, **91**, 14 207–14 211.

——, W. J. Hurlin and A. D. Seigel, 1987: Simulation of the seasonal cycle of the tropical Pacific Ocean. *J. Phys. Oceanogr.*, **17**, 1986–2002.

——, D. Halpern, D. Hansen, R. Legeckis, L. Miller, C. Paul, R. Watts, R. Weisberg and M. Wimbush, 1985: Long waves in the equatorial Pacific Ocean. *Eos, Trans. AGU.*, **66**, 154.

Reid, R. O., B. A. Elliott and D. B. Olson, 1981: Available potential energy: A clarification. *J. Phys. Oceanogr.*, **11**, 15–29.

Regier, L., 1982a: Mesoscale current fields observed with a shipboard profiling acoustic current meter. *J. Phys. Oceanogr.*, **12**, 880–886.

——, 1982b: Error estimates for the Doppler acoustic log used in the NORPAX shuttle experiment, unpublished.

Richardson, P. L., and S. G. H. Philander, 1987: The seasonal variations of surface currents in the tropical Atlantic Ocean: A comparison of ship drift data with results from a general circulation model. *J. Geophys. Res.*, **92**, 715–724.

Semtner, A., and W. Holland, 1980: Numerical simulation of equatorial ocean circulation. Part I: A basic case in turbulent equilibrium. *J. Phys. Oceanogr.*, **10**, 667–693.

Szabo, D., and G. L. Weatherly, 1979: Energetics of the Kuroshio south of Japan. *J. Mar. Res.*, **37,** 531–556.

Talley, L. D., 1983: Radiating instabilities of thin baroclinic jets. *J. Phys. Oceanogr.*, **13,** 2161–2181.

Weisberg, R. H., 1984: Instability waves observed on the equator in the Atlantic Ocean during 1983. *Geophys. Res. Lett.*, **11,** 753–756.

——, 1987: Observations pertinent to instability waves in the equatorial oceans. *Further Progress in Equatorial Oceanography,* E. J. Katz, J. M. Witte, Eds., Nova University Press, 335–350.

Weisberg, R. H., and T. J. Weingartner, 1988: Instability waves in the equatorial Atlantic Ocean. *J. Phys. Oceanogr.*, **18,** 1641–1657.

Williams, R. T., 1980–81: Hawaii-Tahiti Shuttle Experiment CTD Data Rep., Vols. 1–15. SIO Ref. No. 80-22 to 80-36, University of California, La Jolla.

Wilson, D., and A. Leetmaa, 1988: Acoustic Doppler current profiling in the equatorial Pacific in 1984. *J. Geophys. Res.*, **93,** 13 947–13 966.

Wood, R. A., 1988: Unstable waves on oceanic fronts: Large amplitude behavior and mean flow generation. *J. Phys. Oceanogr.*, **18,** 775–787.

Wunsch, C., 1975: Internal tides in the ocean. *Rev. Geophys. Space Phys.*, **13,** 167–182.

Wylie, D. P., B. B. Hinton and M. R. Howland, 1984: Wind stress on the tropical oceans during the year of FGGE. Tech. Rep. University of Wisconsin—Madison.

Wyrtki, K., and G. Meyers, 1975: The trade wind field over the Pacific Ocean. Part I: The mean field and the mean annual variation, Tech. Rep. HIG-75-1. Hawaii Institute of Geophysics.

——, and B. Kilonsky, 1984: Mean water and current structure during the Hawaii-to-Tahiti shuttle experiment. *J. Phys. Oceanogr.*, **14,** 242–254.

——, E. Firing, D. Halpern, R. Knox, G. J. McNally, W. C. Patzert, E. D. Stroup, B. A. Taft and R. Williams, 1981: The Hawaii to Tahiti shuttle experiment. *Science,* **211,** 22–28.